A&A 604, A23 (2017)
DOI: 10.1051/0004-6361/201730810
© ESO 2017

Astronomy & Astrophysics

MUSE-inspired view of the quasar Q2059-360, its Lyman α blob, and its neighborhood*

P. L. North[1], R. A. Marino[2], C. Gorgoni[1], M. Hayes[3], D. Sluse[4], D. Chelouche[5], A. Verhamme[6], S. Cantalupo[2], and F. Courbin[1]

[1] Institute of Physics, Laboratory of Astrophysics, École Polytechnique Fédérale de Lausanne (EPFL), Observatoire de Sauverny, 1290 Versoix, Switzerland
[2] Institute for Astronomy, ETH Zürich, Wolfgang-Pauli Strasse 27, 8093 Zürich, Switzerland
[3] Department of Astronomy, Oskar Klein Centre, Stockholm University, AlbaNova University Centre, 106 91 Stockholm, Sweden
[4] STAR Institute, Quartier Agora, Allée du six Août 19c, 4000 Liège, Belgium
[5] Department of Physics, University of Haifa, Mount Carmel, 31905 Haifa, Israel
[6] Observatoire de Genève, Université de Genève, Ch. des Maillettes 51, 1290 Versoix, Switzerland

Received 17 March 2017 / Accepted 5 May 2017

ABSTRACT

The radio-quiet quasar Q2059-360 at redshift $z = 3.08$ is known to be close to a small Lyman α blob (LAB) and to be absorbed by a proximate damped Lyα (PDLA) system. Here, we present the Multi Unit Spectroscopic Explorer (MUSE) integral field spectroscopy follow-up of this quasi-stellar object (QSO). Our primary goal is to characterize this LAB in detail by mapping it both spatially and spectrally using the Lyα line, and by looking for high-ionization lines to constrain the emission mechanism. Combining the high sensitivity of the MUSE integral field spectrograph mounted on the Yepun telescope at ESO-VLT with the natural coronagraph provided by the PDLA, we map the LAB down to the QSO position, after robust subtraction of QSO light in the spectral domain. In addition to confirming earlier results for the small bright component of the LAB, we unveil a faint filamentary emission protruding to the south over about 80 pkpc (physical kpc); this results in a total size of about 120 pkpc. We derive the velocity field of the LAB (assuming no transfer effects) and map the Lyα line width. Upper limits are set to the flux of the N V λ1238−1242, C IV λ1548−1551, He II λ1640, and C III] λ1548−1551 lines. We have discovered two probable Lyα emitters at the same redshift as the LAB and at projected distances of 265 kpc and 207 kpc from the QSO; their Lyα luminosities might well be enhanced by the QSO radiation. We also find an emission line galaxy at $z = 0.33$ near the line of sight to the QSO. This LAB shares the same general characteristics as the 17 others surrounding radio-quiet QSOs presented previously. However, there are indications that it may be centered on the PDLA galaxy rather than on the QSO.

Key words. galaxies: high-redshift – cosmology: observations – galaxies: active – galaxies: evolution

1. Introduction

Lyman α (Lyα) nebulae have been discovered around many quasi-stellar objects (QSOs) and radio-galaxies at high redshift through slit spectroscopy (Heckman et al. 1991; Lehnert & Becker 1998; Bunker et al. 2003; Villar-Martín et al. 2003; Weidiger et al. 2005; van Breugel et al. 2006; Willott et al. 2011; North et al. 2012), narrow-band imaging (Hu & Cowie 1987; Steidel et al. 2000; Smith & Jarvis 2007; Yang et al. 2014), and more recently, through integral field spectroscopy (hereafter IFS; Christensen et al. 2006; Francis & McDonnell 2006; Herenz et al. 2015; Borisova et al. 2016). They easily span tens of physical kiloparsecs (pkpc) and may be larger than 100 pkpc. Those that host a radio galaxy or a radio-loud QSO are brighter than those hosting a radio-quiet QSO (RQQ), presumably because in the former, interactions between the relativistic jet and the circum-galactic gas enhances ionization (Villar-Martín et al. 2003). The Lyα nebulae surrounding an RQQ or that host no remarkable object are also called Lyα blobs (LABs). Although they do not necessarily host a QSO or active galactic nucleus (AGN), they are found preferentially in overdense regions (Erb et al. 2011; Matsuda et al. 2004, 2009, 2011; Prescott et al. 2008; Yang et al. 2009). These nebulae are interesting because they trace the circum-galactic medium (CGM) at high redshifts, thereby probing galaxy formation, especially if their Lyα fluorescence is enhanced by the ultraviolet (UV) radiation of the QSO, as outlined by Haiman & Rees (2001) and Cantalupo et al. (2005, 2007, 2012).

Although most LABs remain confined within the virial radii of their respective haloes, recent observations have uncovered remarkably large nebulae extending beyond the virial radius (Cantalupo et al. 2014; Martin et al. 2014a,b, 2015; Hennawi et al. 2015), with typical sizes of 400 pkpc. These outstanding observations, some of them made possible by new-generation IFSs like the Palomar Cosmic Web Imager (Martin et al. 2014a,b, 2015), provide the first evidence of the cosmic web filaments predicted by large-scale ΛCDM simulations.

The frequency of LABs around RQQs has remained an open question (e.g., North et al. 2012) until the new-generation IFS Multi Unit Spectroscopic Explorer (MUSE) attached to the fourth unit of the VLT at ESO was used to observe 17 RQQs at redshifts $3 < z < 4$ and found an LAB around each of them

* Based on observations collected at the European Organisation for Astronomical Research in the Southern Hemisphere under ESO programme 60.A-9331(A).

(Borisova et al. 2016, hereafter B16). Therefore, in this redshift range and for a sensitivity of about 10^{-18} erg s^{-1} cm^{-2} arcsec^{-2}, the frequency of LABs surrounding RQQs is 100%. Moreover, the size of such nebulae always reaches or exceeds 100 pkpc, and their surface brightness (SB) profiles are consistent with a power law with a slope of about −1.8.

Obviously, the ubiquity and similarity of the LABs that enshroud RQQs raise the question of their power source and emission mechanism. In addition to fluorescent emission from photoexcitation or photoionization (e.g., Geach et al. 2009), other power sources have been suggested, like cooling radiation where gravitational energy of the gas collapsing in the potential well of the dark matter halo is converted into Lyα radiation after collisional excitation and ionization (known also as the "cold accretion" scenario, see, e.g., Haiman et al. 2000; Fardal et al. 2001; Dijkstra & Loeb 2009; Rosdahl & Blaizot 2012). Shock heating was also proposed (Taniguchi & Shioya 2000; Mori et al. 2004). Finally, scattering of the Lyα photons emitted by a central source (like an AGN) may also occur, betrayed by a high level of linear polarization in the external parts of the nebula (Lee & Ahn 1998; Rybicki & Loeb 1999; Dijkstra & Loeb 2008, 2009; Dijkstra & Kramer 2012). This effect was first observed by Hayes et al. (2011) and may coexist with the cold accretion scenario (Trebitsch et al. 2016). Additional lines such as He IIλ1640 can potentially help distinguish between the cold accretion and the photoionization scenarios, although very deep obervations seem to be needed (Arrigoni Battaia et al. 2015).

Neutral hydrogen clouds may lie on the line of sight of a QSO and produce a so-called damped Lyman alpha (DLA) absorption system, as soon as the column number density exceeds 2×10^{20} cm^{-2}. When the velocity difference between the DLA and the background QSO is $\Delta v < 3000$ km s^{-1}, the two objects are considered as being "associated" and the DLA is then classified as a proximate damped Lyman alpha (PDLA) system (Ellison et al. 2002, 2010). Even though the association may not be physical in the gravitational sense, it can be manifested through enhanced incidence of highly ionized species, for example, showing that the absorber is "influenced by the radiation field of the QSO", as Richards (2001) phrased it. The frequency of PDLAs is close to 2% of the QSOs observed in the redshift range $2.2 < z < 5$, and at redshift 3, it exceeds the frequency expected assuming that they are drawn from the same population as the intervening DLAs (Prochaska et al. 2008; Ellison et al. 2010). In addition to its intrinsic interest, a PDLA provides the advantage of acting like a natural coronagraph that extincts the QSO light in the vicinity of the Lyα line, allowing us to detect and study any emission nebula surrounding the QSO more easily (Hennawi et al. 2009). This configuration, where the PDLA lies in front of the QSO and its Lyα nebula, in principle offers the possibility to "image the PDLA *in silhouette* against the extended screen of Lyα emission", as outlined by Hennawi et al. (2009).

In this work we focus on an LAB lying along the line of sight of the QSO Q2059-360 (RA $21^{\rm h}\ 02^{\rm m}\ 44\overset{\rm s}{.}7$, Dec $-35°\ 53'\ 06.5''$, $V = 18.6$) at redshift $z = 3.09$ (Warren et al. 1991)[1]. The LAB is emitting at ~4970 Å, within the damped Lyα absorption (DLA) trough of the QSO spectrum. The DLA that we analyze in this work is at redshift $z_{\rm abs} = 3.082$, that is, only ~500 km s^{-1} from the background QSO, if the latter is indeed at redshift $z = 3.09$; our revised redshift estimate is rather $z = 3.092$−3.095 (see Sects. 3.1 and 3.3 below), implying a velocity difference of 700−930 km s^{-1} (see Sect. 3.2 below). This would represent 2.3−3.0 proper Mpc if the velocity difference were entirely due to the Hubble flow[2]. An early study of this QSO and of its Lyα features has been carried out by Leibundgut & Robertson (1999). Based on long-slit spectra, they showed that the emission feature is extended both spatially and spectrally, and they provided evidence for a shift of the central wavelength as a function of the offset position from the QSO. Here, we take advantage of the IFS to provide a detailed 2D mapping of the structure.

In our analysis, we assume a ΛCDM universe model with parameters $H_0 = 69.6$ km s^{-1} Mpc^{-1}, $\Omega_{\rm M} = 0.286$, and $\Omega_\Lambda = 0.714$ (Bennett et al. 2014), and we use the cosmology calculator made available by Wright (2006) on the World Wide Web[3].

2. Observations and data reduction

The MUSE instrument is an IFS located at the Nasmyth B focus of Yepun, the VLT UT4 telescope. It is operating in the visible wavelength range from 4800 Å to 9400 Å. Thanks to its wide field of view, $1' \times 1'$ in the wide field mode, it is able to take 90 000 simultaneous spectra with a spatial sampling of $0.2''$ per pixel (also referred to as "spaxel"). MUSE has a resolving power $R = 1835$ (Richard & Bacon 2014) at the redshifted Lyα wavelength, which in terms of velocity separation corresponds to a resolution Δv of

$$\Delta v = c/R \approx 163 \text{ km s}^{-1}$$

where c is the speed of light in the air. Or equivalently in terms of wavelength,

$$\Delta\lambda = \lambda/R \approx 2.7 \text{ Å},$$

where $\lambda \sim 4970$ Å is the wavelength of the Lyα blob emission at redshift 3.08.

The observations were made in June 2014 during the science verification phase (ESO program 60.A-9331(A)). The total exposure time amounts to 3 h 20 min, distributed in four observing blocks, each of which included two 1497 s exposures taken at instrumental position angles differing by 90°. Dithering of a few arcseconds was also applied.

The data set was reduced using both the ESO MUSE pipeline (version 1.6, Weilbacher 2015) and the CubExtractor package (CubEx hereafter, version 1.6; Cantalupo, in preparation). In particular, the basic reduction steps of bias and flat-fielding corrections, wavelength solution, illumination correction, and flux calibration were made for each of the individual exposures with the ESO pipeline using the default parameters. After the calibration files were processed, the raw science data were then reduced using the *scibasic* and *scipost* recipes in order to obtain the datacubes and pixel tables for each exposure sampled in a common grid of $0.2'' \times 0.2'' \times 1.25$ Å. Then, we made use of the CubEx package to compute a more accurate astrometry, to improve the quality of the flat-field correction (CubeFix tool), and to perform a flux-conserving sky subtraction on the individual flatfield-corrected cubes (CubeSharp). We refer to B16 for a detailed description of the CubEx package. Finally, the eight individual exposures were combined into a final cube using a 3σ clipping and mean statistics. The resulting point-spread function (PSF) measured at 7000 Å on the final combined cube has

[1] This is the original reference. The redshift value is mentioned as uncertain for this particular object, while the average error of most other objects is announced to be better than 0.01.

[2] http://home.fnal.gov/~gnedin/cc/

[3] http://www.astro.ucla.edu/~wright/CosmoCalc.html

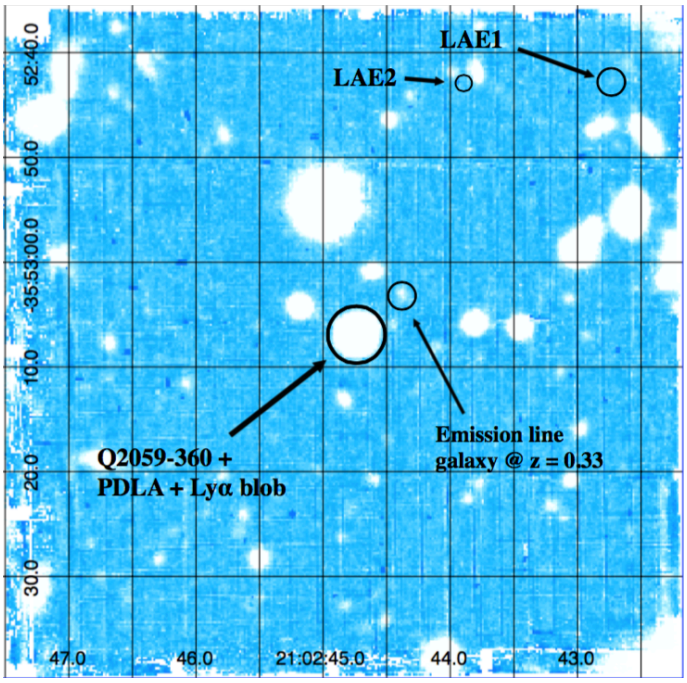

Fig. 1. White-light image obtained by integrating the datacube from 4980 Å to 9350 Å. The positions of the four objects discussed in this paper are indicated. The field of view is one arcminute on a side.

a full-width at half-maximum (FWHM) of 1.03″. At the wavelength of the emitter (4968 Å), it is 1.06″.

The white-light image obtained by collapsing the datacube along the wavelength axis from 4980 Å to 9350 Å is shown in Fig. 1. The position of the QSO is indicated, as well as that of the LAEs found at same redshift, and of an emission line galaxy at $z = 0.33$. We examine these four objects in turn below.

3. Analysis of the datacube in the QSO vicinity

First of all, we have redetermined the redshift of the QSO (Sect. 3.1), and the redhift of the PDLA using metallic absorption lines (Sect. 3.2). Then, we have performed two independent analyses of the immediate neighborhood of the QSO, aimed first at characterizing the LAB. The analysis is complicated by the velocity offset between the PDLA absorption trough and the nebular emission, causing the latter to fall not in the middle of the former, but on its red wing. Thus, the QSO contribution has to be subtracted, even though it remains relatively small, at least in its immediate vicinity, namely within 1″–2″ of it. We used the method proposed by Leibundgut & Robertson (1999), which consists of defining the QSO intrinsic spectrum and subtract it in the wavelength domain for each spaxel; for the sake of consistency, we also performed an analysis similar to that presented by B16 (subtraction of the QSO PSF in the spatial plane for each relevant wavelength bin). We describe these two methods in more detail below (Sects. 3.3 and 4.1).

3.1. Redshift of the QSO

We compared the QSO spectrum extracted from the MUSE datacube with the template QSO spectrum built by Vanden Berk et al. (2001) on the basis of SDSS spectra. The latter have about the same resolution as MUSE, making them appropriate for the task. The most useful emission line for redshift determination is C IVλ1549, although other features such as Si IVλ1396/O IV]λ1402 and C III]λ1908/Fe III can also help. After enhancing the line amplitude with respect to the continuum in the template spectrum (by a factor of 1.8 for C IV and 1.2 for C III]), the best visual match is obtained for

$$z \approx 3.095 \pm 0.003, \tag{1}$$

as shown in Fig. 2 This is slightly larger than $z = 3.09$ estimated by Warren et al. (1991), but within their 0.01 error bar. Our redshift estimate is largely based on the C IV line, which is blueshifted on average by 810 km s^{-1} with respect to the systemic velocity for radio-quiet quasars (Richards et al. 2011); however, this should also be the case of the template spectrum, so this is not likely to cause any severe bias.

3.2. Redshift of the PDLA according to metallic absorption lines

Ten metallic absorption lines can be easily identified in the PDLA system within the MUSE spectral range. These are Si II 1193, Si III 1206, N V 1238, Si II 1260, O I 1302, Si II 1304, C II 1334, Si II 1526, Fe II 1608, and Al II 1670. The N V 1238 line is the faintest of all and has the largest residual from the regression of observed versus laboratory wavelengths, so we discarded it. We also discarded the C IV 1548−1550 lines because they fall in the middle of telluric lines. The difference between the observed wavelength corrected for the air refraction index ($n_{\rm air} \sim 1.00205$) and the redshifted vacuum wavelength is shown in Fig. 3. A least-squares fit weighted by the observed equivalent widths (EW) of the nine lines gives a redshift

$$z_{\rm abs} = 3.08226 \pm 0.00030 \tag{2}$$

with an rms scatter of 0.127 Å, much smaller than the spectral resolution. Our estimate agrees with the value of 3.08303 given by Leibundgut & Robertson (1999) (based on the Fe II 1144, Si II 1193, and Si III 1206 lines) to within 1.5σ.

There is no sign of any multiple absorption components.

The redshift difference of the PDLA relative to the QSO can be translated into a velocity difference using the formulae given by Davis & Scrimgeour (2014): an object with a "peculiar" redshift z_p with respect to a QSO at redshift z_{em} will appear to the observer to have z such that

$$1 + z = (1 + z_{em})(1 + z_p) \implies z_p = \frac{z - z_{em}}{1 + z_{em}} \approx -0.00311. \tag{3}$$

The peculiar velocity v_p is linked to z_p in the following way for relativistic and non-relativistic velocities, respectively:

$$v_p = c\,\frac{(1 + z_p)^2 - 1}{(1 + z_p)^2 + 1} \simeq c\,z_p = -930 \pm 220 \text{ km s}^{-1}, \tag{4}$$

where the error reflects the uncertainty on the QSO redshift. Thus we have $|v_p| < 3000$ km s^{-1}, justifying the classification of the absorption system as a PDLA.

3.3. Fit of the Lyman alpha absorption trough and subtraction of the QSO contribution

From the whole datacube given by the pipeline, we wish to extract the spectrum of the LAB alone in the vicinity of the QSO. The goal is then to subtract the absorption profile from the observed spectrum to obtain a clear signal of the emission feature

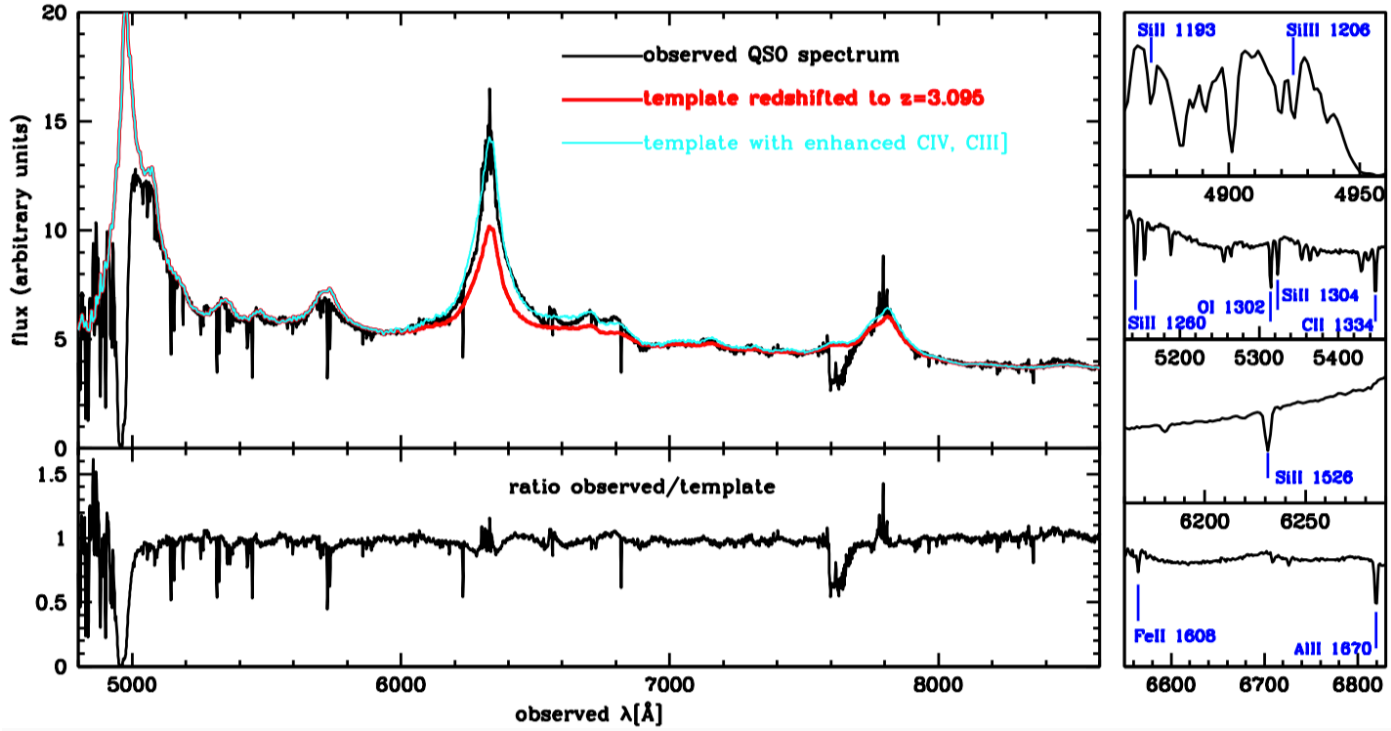

Fig. 2. *Top left*: observed QSO spectrum (black curve) compared to the normalized SDSS template of Vanden Berk et al. (2001) redshifted to $z = 3.095$ (red curve), and to the same template after enhancement of the carbon emission lines (cyan curve, see text). *Bottom left*: ratio of the observed QSO spectrum to the redshifted and normalized template with enhanced C lines. *Right panels*: enlarged portions of the QSO spectrum showing the metallic lines used to determine the redshift of the PDLA.

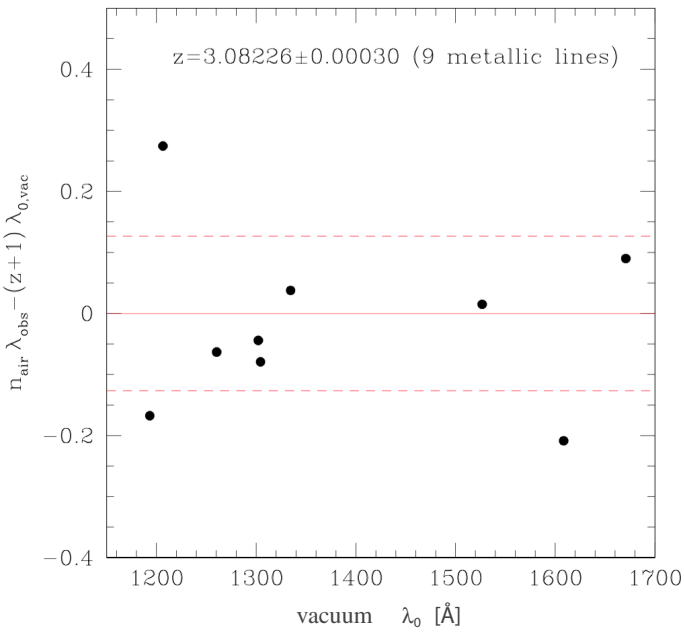

Fig. 3. Difference between the observed wavelength corrected for the air refraction index and the redshifted laboratory (vacuum) wavelength versus laboratory wavelength for the nine lines mentioned in the text. The red horizontal solid line corresponds to the EW-weighted regression, while the red dashed lines show the $\pm 1\sigma$ rms scatter.

without the contribution of the QSO. We first used the `ds9` tool to determine the position of the LAB and roughly estimate its extent. This allowed us to select a region encompassing most of the LAB luminosity, and of course the whole QSO contribution. The region we selected is elliptical, with semi-axes of 2.3″ and 2.8″, the position angle (orientation with respect to the north direction, counted positively to the east) of the semi-major axis being 30°. The procedure to isolate the spectrum of the LAB is then the following:

- We use the software `VPFit` (Carswell & Webb 2014) to fit a Voigt profile to the absorption trough. The needed error vector was extracted from the variance datacube, and we dropped all irrelevant data, namely (i) absorption lines of the Lyα forest, on the blue side of the DLA trough; (ii) some faint absorption features to the red side of the DLA trough (5000 Å $< \lambda <$ 5100 Å); (iii) some narrow absorption lines on the blue wing of the DLA trough (~4930 Å $< \lambda <$ 4940 Å); and (iv) the Lyα blob emission. These regions are shown in Fig. 4.
  In order to obtain a meaningful fit, we need to reconstruct the original energy distribution of the QSO (we call it "the continuum" somewhat abusively, because here lies the broad Lyα line). This is done by iteration over the following steps:
- We start by performing a first fit, feeding `VPFit` with our measured spectrum (blue curve in Fig. 4) and a preliminary continuum (close to the green curve in Fig. 4). `VPFit` will then provide a Voigt profile fit of the DLA.
- We divide the original spectrum by the DLA fit, obtaining the function f_r shown in Fig. 5 (blue line). The upper envelope of f_r should tend toward 1 outside the emission region of the LAB (and outside the bottom of the absorption trough) because one has to ensure that the wings of the Lyα absorption are well fitted, regardless of the other absorption lines. The closer f_r is to 1, the better is the continuum.
- We then manually define the upper envelope of the f_r function, neglecting both the bottom of the PDLA absorption (where f_r is not defined) and the LAB emission (see Fig. 5,

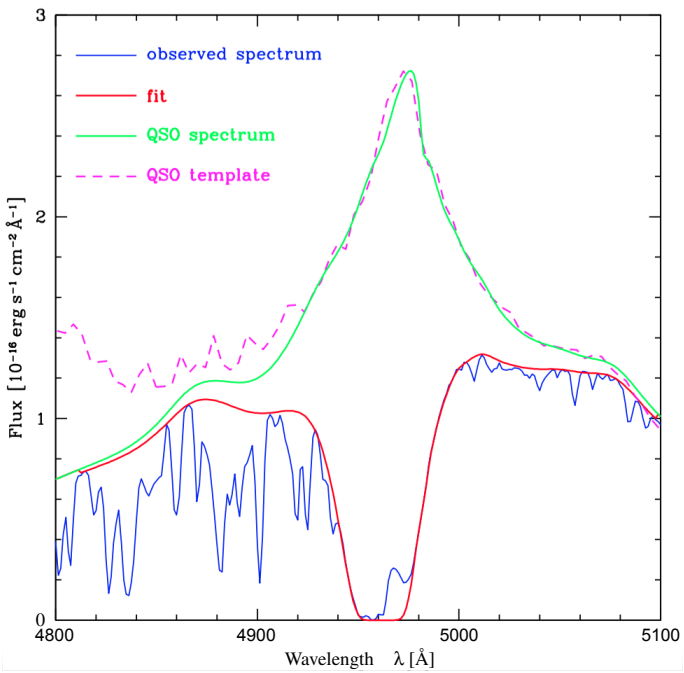

Fig. 4. QSO spectrum with the Lyα DLA feature. The blue line is the measured spectrum, with the emission feature at the bottom of the damped Lyα absorption trough. The Lyα forest lies on the blue side of the DLA Lyα absorption. The red curve shows the Voigt fit of the DLA. The green curve is the reconstructed "continuum", actually the broad Lyα emission line of the QSO (see text). Note that the reconstructed QSO line is only an interpolated guess between ~4950 Å and ~4958 Å. The thin dashed magenta line is the SDSS QSO template of Vanden Berk et al. (2001) redshifted to $z = 3.092$ and normalized to match the green curve as well as possible.

red line). This provides a vector by which we multiply the previous estimate of the continuum to obtain an improved estimae. We note that by construction, this vector remains uncertain in the wavelength range ~4948–4977 Å, where we are forced to interpolate the continuum. If the latter were to present any discontinuity or peak within that range, neither this method nor any other would be able to unveil it.

Four such iterations allowed us to converge to a satisfactory fit of the QSO+PDLA spectrum, shown in Fig. 4. We note that the shape of the resulting broad emission Lyα line is remarkably close to that of the template spectrum, after the latter has been properly normalized (i.e., divided by the linear function $y = 0.0035 \cdot \lambda\,[\text{Å}] - 10.821$).

We can now scale the fitted spectrum and subtract it from the observed spectrum in each spaxel concerned by the QSO contribution. This is done in the following way. Let $I_{\rm ref}$ be the spectrum extracted in the first part (the blue curve in Fig. 4), and s_{ij} the spectrum in a particular spaxel located at position (i, j) in the image. The scaling factor h_{ij} for a specific spectrum is given by the ratio between the sum of s_{ij}, selected in a small wavelength range $D_\lambda = [5018.75\,\text{Å}, 5036.25\,\text{Å}]$ where the spectrum is nearly flat, and the sum of $I_{\rm ref}$ in the same range:

$$h_{ij} = \frac{\sum_{\lambda \in D_\lambda} s_{ij}(\lambda)\Delta\lambda}{\sum_{\lambda \in D_\lambda} I_{\rm ref}(\lambda)\Delta\lambda}, \tag{5}$$

where $\Delta\lambda = 1.25$ Å is the spectral sampling of our image. Thanks to the scaling factor, we can estimate a fit for the PDLA profile in each spaxel. If $F_{\rm ref}$ is the QSO+PDLA spectrum computed above (red curve in Fig. 4), the QSO+PDLA spectrum f_{ij} in each spaxel is given by

$$f_{ij} = h_{ij} F_{\rm ref}. \tag{6}$$

Therefore, the LAB spectrum $\tilde{s}_{ij}$ in each spaxel, without the QSO contribution, is given by subtracting the estimated fit f_{ij} to the measured spectrum s_{ij}:

$$\tilde{s}_{ij} = s_{ij} - f_{ij}. \tag{7}$$

We now have a new subcube $\tilde{s}_{ij}$ from which the signal of the QSO has been subtracted.

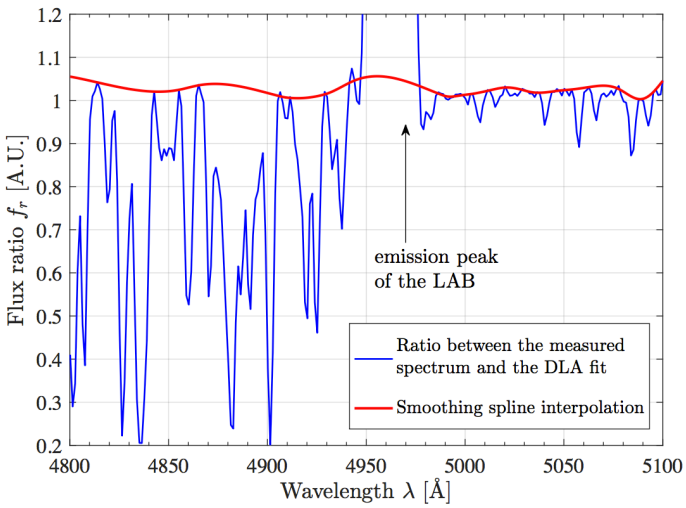

Fig. 5. Illustration of the second and third step of the procedure for estimating the QSO continuum. The highest values of f_r (blue curve) must tend to 1 (outside the bottom of the PDLA absorption and the LAB emission), when the profile for the DLA converges to a good solution; the blue curve diverges in the wavelength range corresponding to the bottom of the PDLA absorption and to the LAB emission, where it has to be interpolated. The red curve shows the spline interpolation performed over the highest points of the blue curve. The spline function has then to be multiplied by the previous estimate of the continuum to create a better estimate.

4. Exploration of the datacube at larger scales

We have explored the datacube at scales larger than just a few arcseconds from the QSO, both visually and in an automated way.

Visual exploration was made by scanning the cube in increasing wavelength bins and by displaying the spectrum of the few emission line objects that were detected. It also allowed us to discover a faint extension of the LAB protruding to the south-southwest for some 10″.

Automated exploration aimed at defining the extension of the LAB in a more objective and sensitive way was performed with CubEx, which in addition to its post-processing capabilities, is also able to exploit simultaneously the 3D information of the datacube to automatically extract extended emission above some predefined signal to noise ratio (S/N) threshold. More details are given hereafter and by B16. This method allowed us to deeply explore the filamentary structure we had assumed to be there based on visual exploration, which is oriented to the south over more than 10″ (~100 pkpc), and to better define its shape and surface brightness.

4.1. PSF quasar subtraction from each monochromatic image

We also explored an alternative empirical method that is implemented in CubEx to minimize the contribution of the QSO PSF and obtain the "pure" extended Lyman alpha emission. The principle of this method has been widely used in imaging astronomy (Husemann et al. 2013) and is very well suited to IFS data (Herenz et al. 2015). In summary, an empirical PSF is scaled and subtracted from the QSO at each wavelength layer. We used the CubePSFSub tool, which is also part of the CubEx package, to create the pseudo-NB images (150 spectral pixels or 187 Å) at the position of the QSO, then the flux measured in the 1″ × 1″ central region was rescaled in each empirical PSF image and finally subtracted from the corresponding wavelength layer in the datacube (see Sect. 3.1 in B16 for further details). Although this method produces excellent results far away from the quasar, it does not provide robust results in the central 1″ region. Ultimately, we used the latter CubEx approach to detect the extended LAB and the approach described in Sect. 3.3 to study the PDLA properties.

5. Results

5.1. Properties of the PDLA and of the bright component of the Lyman alpha blob

We first focus on the properties of the PDLA obtained through the `VPFit` code. Together with the fitted absorption profile, both the column density and the redshift of the PDLA are derived:

$$\log(N) = 20.9290 \pm 0.0024; \quad z_{\rm abs} = 3.082097 \pm 0.000053. \quad (8)$$

The redshift value obtained here differs by no more than 0.000163 from the value obtained based on metallic lines and is thus entirely consistent with it (see Sect. 3.2 above). We took the refractive index n of air into account that causes a shift in the observed wavelengths: $\lambda_{\rm air} = \lambda_{\rm vac}/n$. We used the Ciddor equation (Ciddor 1996), taking the atmospheric conditions at the time of the measurement into account (air temperature 12°C, pressure 744.9 hPa, and relative humidity 3%, as reported in the header of the original FITS file). The errors are the formal errors provided by `VPFit` and are certainly underestimated, as they do not include uncertainties linked to the continuum determination. In their pioneer study, Leibundgut & Robertson (1999) obtained a column density and redshift

$$\log(N) = 20.85 \pm 0.03; \quad z_{\rm abs} = 3.0825.$$

Our estimate of the column density is higher than theirs by 2.6σ (referring to their error estimate), and we find a slightly lower redshift (the difference amounts to 7.6σ according to our own error estimate). The latter discrepancy might be due to our lower spectral resolution ($R \sim 1840$ instead of 3300), which might cause the metallic absorption lines in the blue wing of the Lyα absorption trough to be less easily recognized and be partly included in the Voigt profile fit. This would result in a slightly overestimated column densitiy and in a slight blue shift. However, our `VPFit` estimate of the redshift, based on the Lyα line alone, agrees within only 0.5σ with the PDLA redshift estimate based on metallic lines.

We can determine the average spectral shape of the LAB emission feature over the 4.6″ × 5.6″ elliptic surface defined previously by subtracting the DLA fit to the measured spectrum. The result, shown in Fig. 6, is a clearly asymmetric line that can formally be fitted by a pair of Gaussian functions (Fig. 6). The parameters of the two Gaussians are listed in Table 1. We note that these two functions are only used as a convenient way of representing the average emission line and do not bear straightforward physical meaning. The total Lyα flux $F_{\rm Ly\alpha}$ of the emission feature is computed by integrating the flux over the double Gaussian profile:

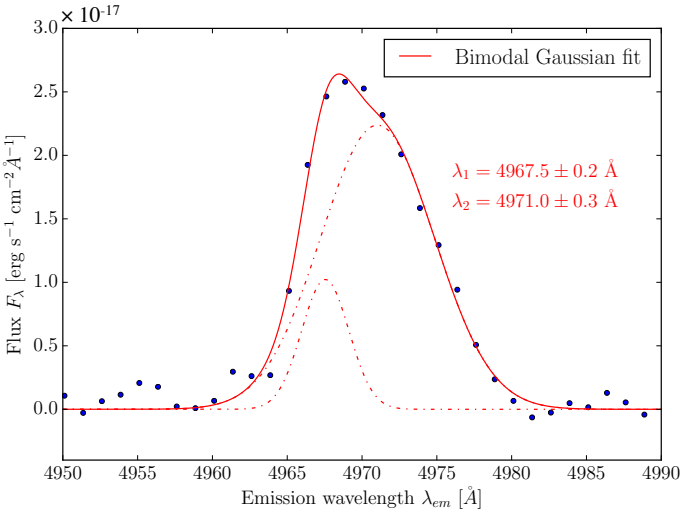

Fig. 6. Spectrum of the emission feature averaged over an elliptic surface of 2.3″ × 2.8″, centered on the QSO, but free of its flux. The heavy continuous curve is a fit performed with the sum of two Gaussians (dash-dotted lines). The wavelengths indicated are corrected to vacuum.

Table 1. Central position λ (corrected to vacuum) and FWHM of the two Gaussian components in the LAB spectrum.

	λ [Å]	*FWHM* [km s^{-1}]	*FWHM* [Å]
first peak	4967.5 ± 0.2	225 ± 42	3.7 ± 0.7
second peak	4971.0 ± 0.3	538 ± 24	8.9 ± 0.4
first moment	4970.5 ± 0.1	559 ± 12	9.27 ± 0.20

Notes. The third line gives the same quantities for the total emission profile.

$$F_{\rm Ly\alpha} = (2.53 \pm 0.05) \times 10^{-16}\ {\rm erg\ s^{-1}\ cm^{-2}}. \quad (9)$$

The mean redshift of the LAB is defined as

$$z = \frac{\lambda_{em} - \lambda_0}{\lambda_0} = 3.0887 \pm 0.0001, \quad (10)$$

where $\lambda_0 = 1215.67$ Å is the Lyα wavelength at rest (in the vacuum) and λ_{em} is the observed wavelength of the emission corrected to vacuum. The (vacuum) wavelength $\lambda_{em} = 4970.5 \pm 0.1$ Å is determined by the first-order moment of the distribution. This is a reasonable choice because it takes the skewness in the shape of the spectrum into account. The redshift of this bright central part of the LAB is therefore very close to but different from that of the QSO: the difference amounts to $z_p = -0.00154$ or -462 km s^{-1}, about twice the uncertainty on the QSO redshift (assuming $z_{\rm QSO} = 3.095 \pm 0.003$).

The velocity difference between the PDLA and the LAB is then

$$\Delta v = v({\rm PDLA}) - v({\rm LAB}) = -473 \pm 24\ {\rm km\,s^{-1}},$$

in perfect agreement with the -490 km s^{-1} given by Leibundgut & Robertson (1999).

From the redshift, we determine the luminosity distance d_L and the total Lyα luminosity of the blob:

$$L_{\mathrm{Ly}\alpha} = 4\pi d_L^2 F_{\mathrm{Ly}\alpha} = (2.18 \pm 0.05) \times 10^{43} \mathrm{erg\,s^{-1}} \quad (11)$$

with $d_L = 26\,850$ Mpc. The error given here is a formal error provided by the fit; a more realistic error would be closer to ~10%, taking into account the uncertainty of the subtracted QSO spectrum. The FWHM of the average emission spectrum (not corrected for the instrumental width) is:

$$FWHM = 9.27 \pm 0.20\,\text{Å} \quad \text{or} \quad FWHM = 559 \pm 12\,\mathrm{km\,s^{-1}} \quad (12)$$

if we naively admit that the line width reflects the velocity field alone, without any transfer effect. This rather modest value already indicates that the gas is not subject to violent motions, especially as part of the line width may be accounted to transfer effects, making our FWHM estimate an upper limit rather than a true estimate of the kinematics. Leibundgut & Robertson (1999) obtain FWHM values varying from ~300 to ~540 km s^{-1} (or even 650 km s^{-1}, but for a line affected by a cosmic ray), which is clearly smaller. However, their values refer to individual observations of various parts of the LAB, so they do not include the large scale velocity field (or transfer effects). They also use a higher spectral resolution, which tends to decrease the measured FWHM, although this accounts for no more than a difference of ~25 km s^{-1}.

5.1.1. Spatial shape of the central LAB component

Summing the successive layers in the wavelength range of the LAB, we obtain an image of the blob and can determine its extension and shape. In each spaxel at position (i, j) of the resulting stacked image we have the sum of all pixel values $I_{ij}(\lambda)$, located at the same position (i, j), over the interval D_λ ranging from 4950 Å to 4990 Å encompassing the LAB emission:

$$\bar{I}_{ij} = \sum_{\lambda \in D_\lambda} I_{ij}(\lambda)\Delta\lambda. \quad (13)$$

The result is shown in Fig. 7.

The coordinates of the blob center are

$$\mathrm{RA} = 21^{\mathrm{h}}\,02^{\mathrm{m}}\,44.73^{\mathrm{s}}, \quad \mathrm{Dec} = -35^\circ\,53'\,06.9''. \quad (14)$$

We see that this bright LAB component has a roughly circular shape with an extension of about 3″–4″. This corresponds to a diameter of 23–31 kpc at the LAB redshift.

5.1.2. Velocity map of the LAB central part

To create the velocity map of the blob[4], we fit a Gaussian profile on each spectrum $\tilde{s}_{ij}$ of the subcube. From the mean position value of the Gaussian fit, we obtain the redshift z. We wish to obtain the "peculiar" redshift z_p at each location of the blob, however, which has a global redshift $z_{em} = 3.0887$.

By applying relations (3) and (4) to each spectrum of the subcube, we obtain the velocity map of the blob, shown in the left panel of Fig. 8. We can clearly distinguish the presence of two regions, each with a relatively uniform velocity, and separated by a steep north-south gradient from about 80 km s^{-1} at the LAB center, ~0.4″ south of the QSO, to about −100 km s^{-1} 2″ south of the QSO. Leibundgut & Robertson (1999) have shown some evidence for this feature (see their Fig. 4c), but their data could not provide a complete map such as ours, which also shows an east-west velocity gradient ~1″ to the east of the LAB center. We also note that our peculiar velocities overall range from about −120 km s^{-1} to +80 km s^{-1}. This ~200 km s^{-1} difference is not much larger than our spectral resolution, which is ~163 km s^{-1}, but it is quite significant. It agrees well with the ~240 km s^{-1} difference found by Leibundgut & Robertson (1999, Table 2 and Fig. 4).

[4] The "velocity" word used here is a proxy for "line position" and is strictly justified only when transfer effects can be neglected.

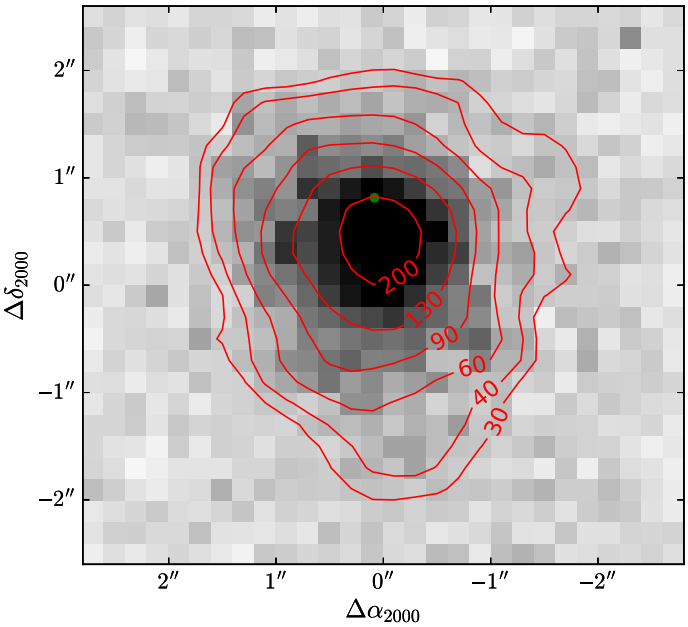

Fig. 7. Image of the LAB obtained by addition of the successive frames from 4950 Å to 4990 Å. The signal of the QSO has been removed, as explained in the text, and the position of the QSO is shown by the green dot. The red curves are isophotes spanning SBs from 30×10^{-20} erg s^{-1} cm^{-2} spaxel^{-1} to 200×10^{-20} erg s^{-1} cm^{-2} spaxel^{-1}, or 7.5×10^{-18} erg s^{-1} cm^{-2} arcsec^{-1} to 5×10^{-17} erg s^{-1} cm^{-2} arcsec^{-1}. The outermost isophote corresponds to $S/N \sim 1.8$, while the inner corresponds to $S/N \sim 12$ per spaxel. There is a slight offset of the QSO position by about 0.4″ with respect to the isophotal center of the blob. The relative coordinates are defined with respect to the field center.

The right panel of Fig. 8 is a map of the FWHM (obtained through the Gaussian fit) of the Lyα emission line. When we consider both panels, a rough overall trend of an increasing FWHM with increasing velocity seems to appear: the FWHM is around 300 km s^{-1} 2″ south of the QSO, but closer to 600 km s^{-1} at the LAB center. This is also consistent with Leibundgut & Robertson (1999, Fig. 4d).

To verify that the different spectra in each spaxel are well fitted by the Gaussian functions, we provide Fig. 9. Each subplot of this figure shows the total flux recorded in each spaxel. The total area of the figure corresponds to the dashed rectangle in Fig. 8. The Gaussian fit appears satisfactory in each subplot where the noise is low enough, which occurs when the fitted amplitude is larger than $\sim 5 \times 10^{-20}$ erg s^{-1} cm^{-2} Å^{-1}.

5.2. Properties of the Lyman alpha blob at larger distance from the QSO and other objects

Using the CubExtractor software, we were able to map the whole LAB, especially at large distance from the QSO, as seen in Fig. 10. The LAB extends over 100 pkpc at least, like the

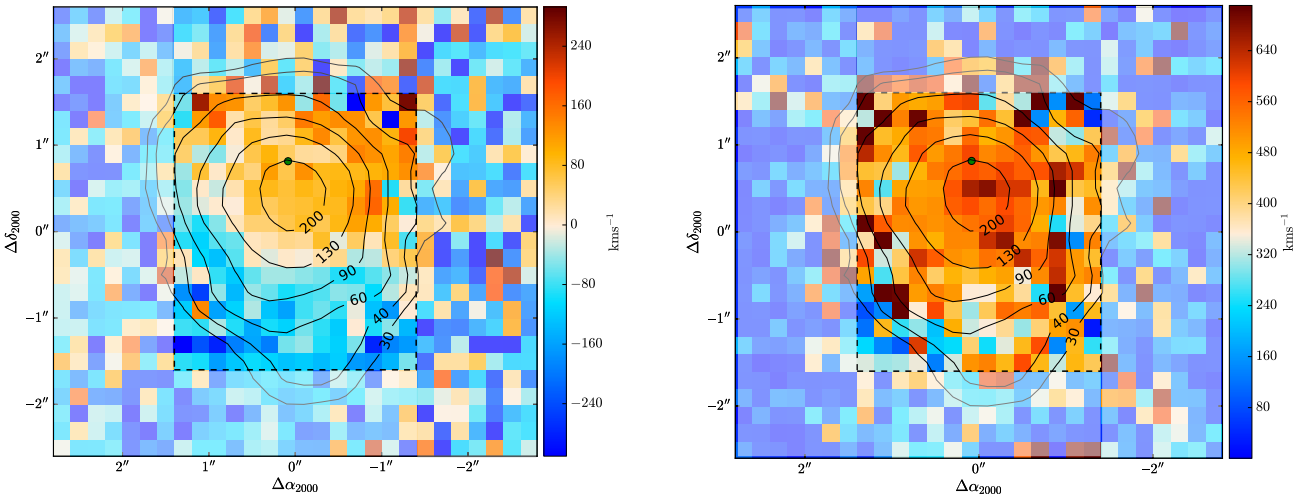

Fig. 8. *Left*: velocity map of the Lyα emission feature. The color code highlights the velocity along the line of sight in each spaxel of the image, the zero-point being set at $z = 3.0887$ or $\lambda_{\rm vac} = 4970.5$ Å. The curves are the isophotes labeled in units of 10^{-20} erg s^{-1} cm^{-2} spaxel^{-1}. Below 6×10^{-19} erg s^{-1} cm^{-2} spaxel^{-1}, the S/N is very low and everything outside this isophote is strongly affected by background noise. The green point near the center shows the position of the QSO. The dashed rectangle represents the region of the image used in Fig. 9; we have enhanced it by lowering the contrast in the area that surrounds it. *Right*: map of the FWHMs of the Lyα emission feature. The FWHM in each spaxel is computed from the Gaussian fit of the emission spectrum. For comparison, the average FWHM measured from the total emission spectrum is 560 km s^{-1}.

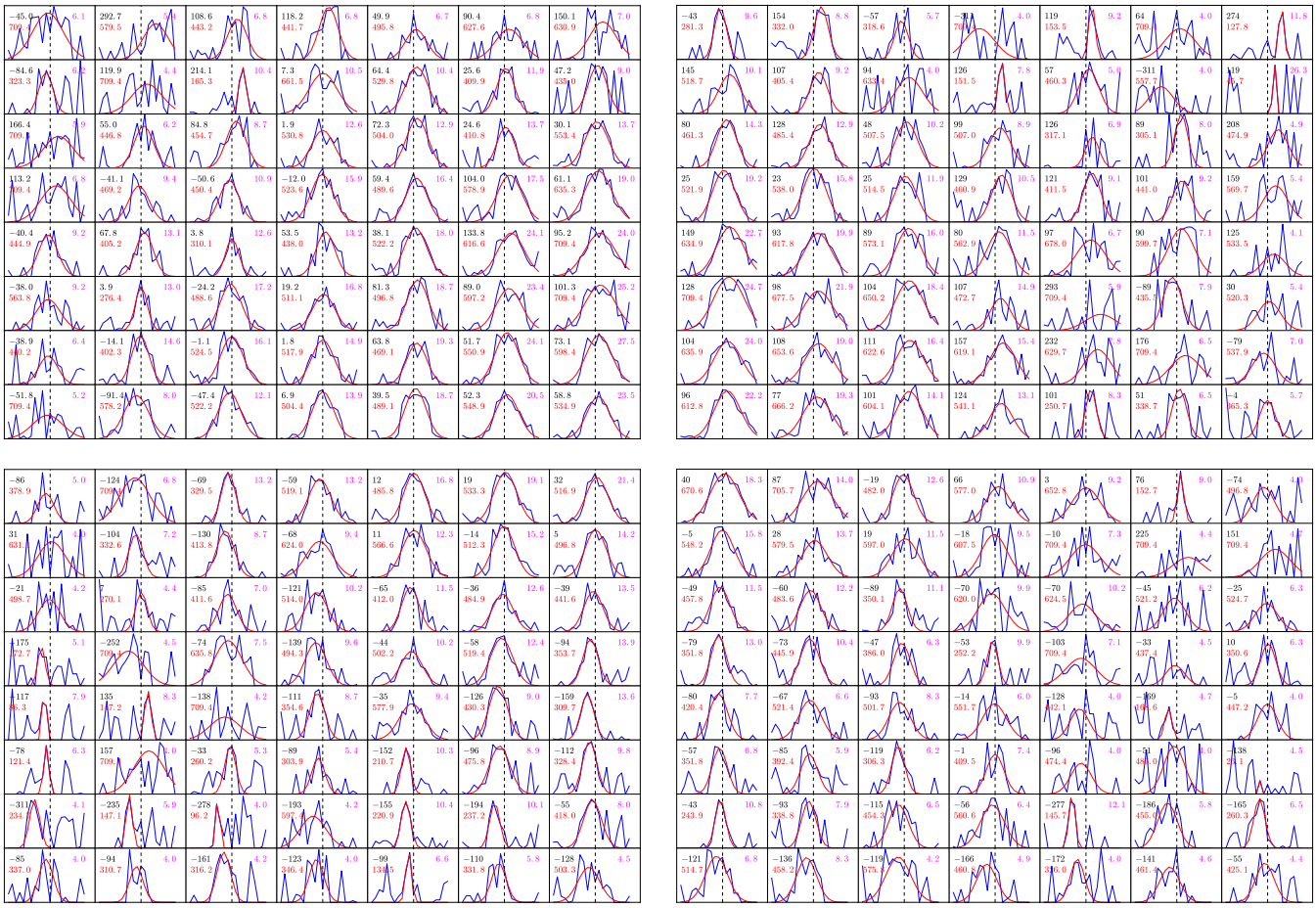

Fig. 9. Map of spectra recorded in individual spaxels. The total area corresponds to the dashed rectangle in Fig. 8; it covers 14 × 16 spaxels (2.8″ × 3.2″). North is up and east to the left. The blue lines show the measured spectra, and the red curves the Gaussian fits. The spectral range is 4955–4980 Å. The black number inside each subplot (*top left corner*) is the peculiar velocity in km s^{-1} computed from the Gaussian fit; the red number just below is the FWHM of the emission line in km s^{-1}; the purple number (*top right*) is the amplitude of the Gaussian in units of 10^{-20} erg s^{-1} cm^{-2} Å^{-1} spaxel^{-1}. The dashed vertical line marks the average emission wavelength (4970.0 Å). The quasar lies in the upper left quadrant, in the spaxel [7, 5] just next to spaxel [7, 4] (where [1, 1] and [7, 8] define the lower left and upper right spaxels).

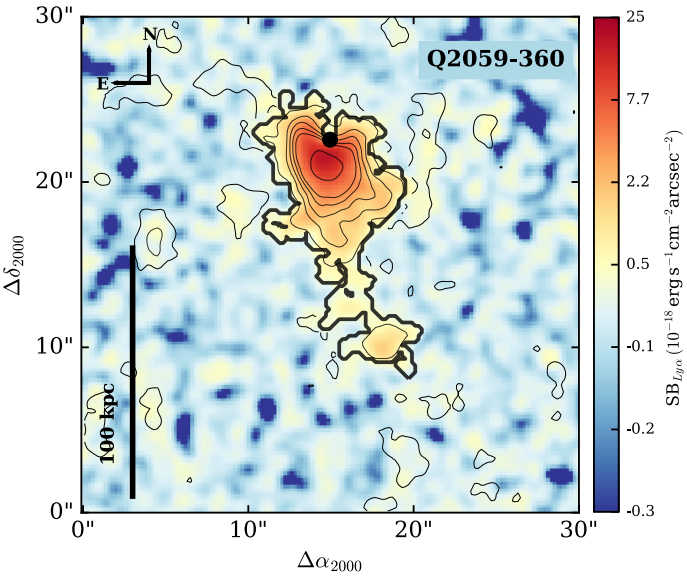

Fig. 10. Optimally extracted map of the LAB, obtained using the CubEx software on the PSF and continuum subtracted MUSE datacube, and by collapsing along the wavelength axis the datacube voxels inside the 3D segmentation map. The spatial projection of the 3D mask is indicated by the thick contour that corresponds to an SB of about 1×10^{-18} erg s^{-1} cm^{-2} arcsec^{-2} and an S/N of 2.3. The thin contours indicate the propagated S/N in the images, the outermost one corresponding to $S/N = 2$ and the other ones to S/Ns increasing by steps of 6 units (see B16 for a detailed explanation). The QSO position is shown by the black dot. Note the long tail extending southward of the QSO; this was unknown to date.

17 other LABs observed around radio-quiet QSOs by B16. The large extension is mainly due to a filament protruding southward and the Lya flux measured within the 3D mask (thick contour) is 1.67×10^{-16} erg s^{-1} cm^{-2}. This is lower than what we found for the bright part of the LAB, probably because of the poor subtraction of the QSO light at the QSO position, which artificially reduces the LAB intensity there. The filament is relatively thin but appears resolved, being wider than 1″ or 8 pkpc.

The morphology of this LAB is quite similar to that of several LABs discovered by Matsuda et al. (2011) through the Subaru Lyα blob survey in the SSA22 area at the same redshift. In particular, SSA22-Sb6-LAB4 has almost exactly the same shape and extent, with a thin filament protruding to the southwest. The only difference is the absence of any obvious QSO.

The corresponding velocity map is shown in the left panel of Fig. 11, the zero velocity corresponding to $\lambda_{\rm vac} = 4967.26$ Å (maximum of the emission intensity), that is, to -196 km s^{-1} in Fig. 8 (left panel). It is based on the first moment of the emission line, while the velocity map of the immediate vicinity of the QSO (Fig. 8) is obtained through Gaussian fits. This might partly explain the larger velocity contrast (~300 km s^{-1} instead of ~200 km s^{-1}) near the QSO. Another cause for the discrepancy may be the approximate subtraction of the QSO PSF. Nevertheless, the two velocity maps agree regarding the north–south velocity gradient, which appears very steep about 1″ south of the QSO.

At larger scale, the southern component of the LAB overall has a velocity close to 0 km s^{-1}, while in the close QSO neighborhood, the velocity is higher than ~100 km s^{-1}.

The map of velocity dispersion (as a proxy for the line width) is shown in the right panel of Fig. 11. We note the very small dispersion in the southern component of the LAB, which is essentially equal to the MUSE resolution limit. The same is true of the southern part of the main LAB component. Near the QSO, the Lyα line is broader on an oblique band stretching from the SW of the QSO to the SE of it. Our previous map (Fig. 8, right panel) does not show this feature so clearly, but does display widths between ~240 and ~600 km s^{-1}, which are similar. There is rough agreement between the two maps in the sense that the Lyα line tends to be broader near the QSO than far away from it.

5.2.1. Surface brightness profile and size–luminosity relation

We show the mean radial variation of the azimuthally averaged surface brightness (SB) in Fig. 12, as measured on the SB map of Fig. 10. The average is taken over circular annuli. Although the LAB is strongly asymmetric, it is worth comparing this radial variation with that of other blobs. As mentioned above, the innermost part (radius $\lesssim$1″) is not reliable, but the rest is, and the SB curve shown here was obtained in exactly the same way as the 17 others published by B16. It is essentially free of any pollution from the QSO light because it shows only the result beyond 10 kpc of it, that is, beyond 1.3″. The red line shows a power-law fit (see B16, Appendix B) with an index $\alpha = -1.51$, slightly lower than the average shown by the purple line and corresponding to $\alpha = -1.8$. Only four of the 19 objects (including two nebulae associated with radio loud QSOs) of B16 have a shallower profile. The exceptionally elongated and filamentary shape of our LAB might be responsible for this unusual profile.

Figure 12 also shows the SB profile of the Slug Nebula (Cantalupo et al. 2014). We see that in the range of radii considered, the profile of our LAB lies almost an order of magnitude below the average of the B16 sample. Overall, our LAB compares well with the sample of B16, even though it lies on the faint side.

This is also confirmed by the relation between luminosity and size shown in Fig. 14. The size is defined here as the major axis of the nebula. The objects observed by B16 are represented as blue stars, while the full magenta dots are the LABs discovered by Matsuda et al. (2011). Interestingly, the latter largely overlap the former, but extend to lower luminosities and smaller sizes. This is probably an observational bias: B16 have selected the brightest QSOs, so one may expect that the luminosity of the associated LABs is enhanced by fluorescence due to the QSO UV radiation. On the other hand, Matsuda's LABs do not harbor any obvious QSO. Thus, our object indeed lies on the faint end of the LABs surrounding bright QSOs, but appears to be a rather average one when compared to the general LAB population, as far as the sample of Matsuda et al. (2011) is representative.

5.3. Upper limits to high-ionization lines

We examined the QSO-subtracted datacube for any presence of the N Vλ1238.8−1242.8, C IVλ1548.2−1550.8, He IIλ1640.4, and C III]λ1908.7. We defined 2σ upper limits to the flux of these lines, using the same method as in B16, and compared them with the flux of the Lyα line defined in the same datacube. The results are given in Table 2, and Fig. 13 shows the ratio of the He II and Lyα fluxes versus the ratio of the C IV and Lyα fluxes for our object and for the B16 sample. Here again, our object appears quite similar to the other nebulae found around radio quiet QSOs. Arrigoni Battaia et al. (2015) have shown that in order to rule out the photoionization scenario, one would need to reach upper limits as low as 0.05 and 0.07 on the He II/Lyα and

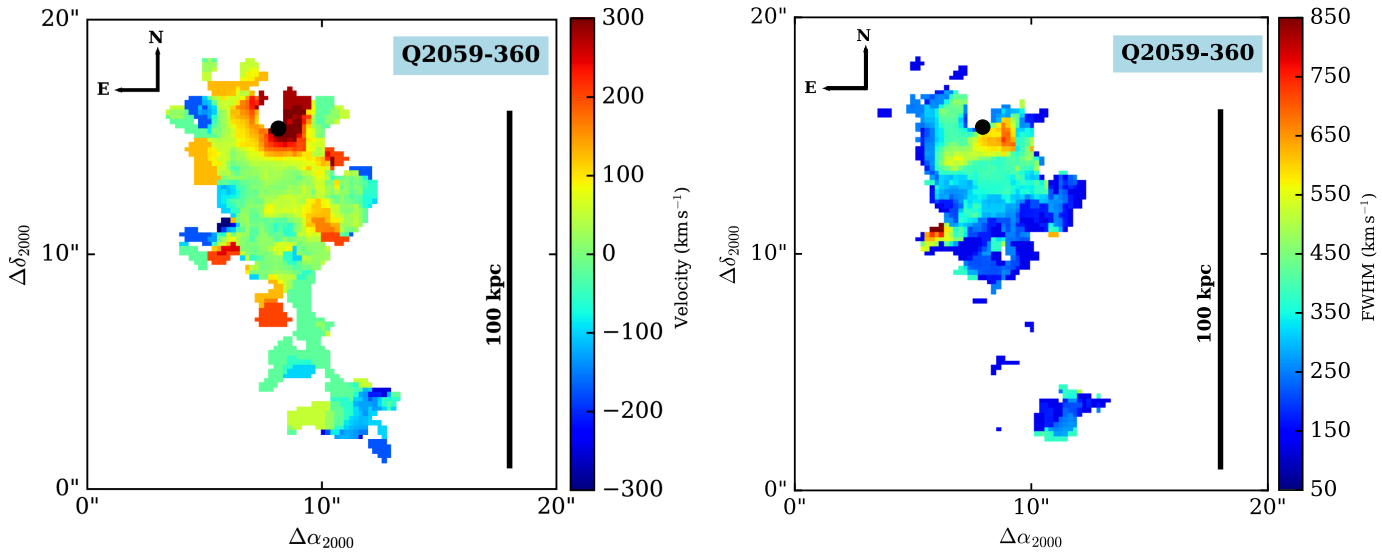

Fig. 11. *Left*: large-scale velocity map of the LAB given by the CubEx software on the basis of the first moment of the Lyα emission line. The QSO position is marked by the black dot. The zero velocity corresponds to $\lambda_{\rm vac}$ = 4967.26 Å, or to −196 km s^{-1} in Fig. 8 (left panel). *Right*: large-scale map of the velocity dispersion in the LAB given by the CubEx software on the basis of the second moment of the Lyα emission line.

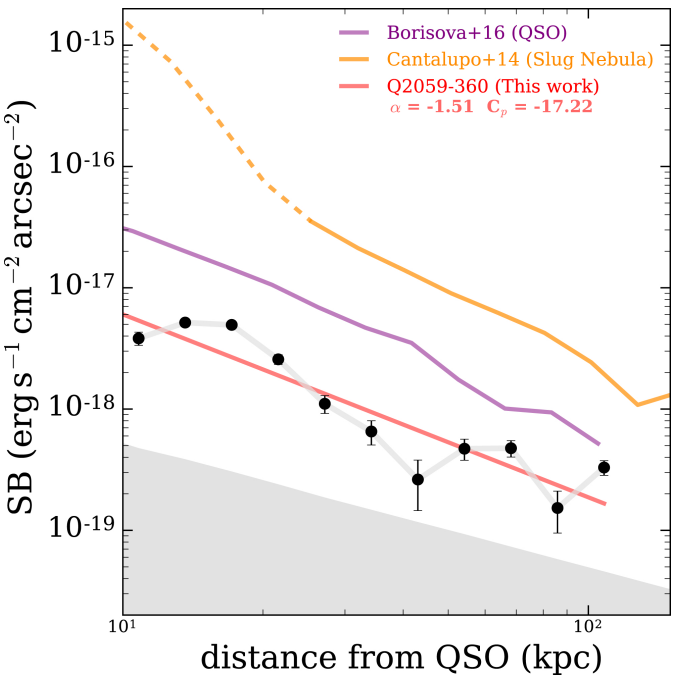

Fig. 12. Radial variation of the SB of the LAB (black dots; distance in physical kpc). The red line is a least-squares fit of a power law to the data. The average profile of the 17 nebulae associated with radio-quiet QSOs (B16) is shown as a purple line. The yellow line represents the Slug Nebula (Cantalupo et al. 2014), the dashed part of it is polluted by the QSO light. Correcting the observed SB for redshift dimming would bring the yellow curve very close to the purple curve, but would slightly increase the distance between the red and purple curves. The upper limit of the gray area corresponds to the 2σ noise on the profile.

C IV/Lyα ratios, respectively. This is indicated by the green area in Fig. 13: photoionization as modeled by Arrigoni Battaia et al. (2015) is possible within that area, but would imply unrealistic hydrogen column densities (>10^{22} cm^{-2}) beyond it (the authors assume spherical clouds of cool gas). None of the high-ionization lines available in the MUSE spectral range can be seen, and our upper limit on the C IV/Lyα flux ratio seems

Table 2. Upper limits to the SB of lines due to highly ionized species.

Line, λ (vac.) [Å]	Flux (2σ limit) [10^{-18} erg/s/cm^2/arcsec^2]	$\frac{\rm Flux(line)}{F({\rm Ly}\alpha)}$
N V 1238.8−1242.8	<10.3	0.058
C IV 1548.2−1550.8	<6.7	0.038
He II 1640.4	<7.1	0.040
C III] 1908.7	<22.1	0.125

compelling enough to exclude photoionization by the QSO as the main driver of the LAB Lyα luminosity. The upper limit on the He II/Lyα ratio is just below the border mentioned, so that based on this criterion alone, our object would be on the verge of being compatible with photoionization by the central source. Interestingly, only one among the B16 radio quiet targets lies in the photoionization region in Fig. 13, but since its position corresponds to upper limits only, it remains impossible to tell how far its luminosity can really be explained by photoionization. All other objects have a too low line ratio along either one or both axes.

5.3.1. Two other probable Lyman alpha emitters at the same redshift

We have detected two other possible Lyα emission features in the neighborhood of the QSO; their coordinates are given in Table 3.

The brighter feature (LAE1) lies 34″ away from the QSO, which corresponds to a projected distance of about 265 pkpc, and it emits within the range 4960 Å to 4975 Å. The vicinity to the QSO and the emission at wavelengths identical to the central LAB suggest that this object is emitting in the Lyα line. Figure 15 (left panel) shows the extension of this emitter as found with CubEx, which is about 4.3″ or 34 pkpc in diameter; if the eastern extension is real and physically belongs to the LAE, then the major axis of the LAE would reach 6.4″ or 50 pkpc. This appears very large, but is consistent with the finding of Wisotzki et al. (2016), who found many examples of LAEs with Lyα emission extending to 2″ radius at similar redshift.

The emission feature of this nebula consists of two peaks, as shown in the right panel of Fig. 15. This is very typical

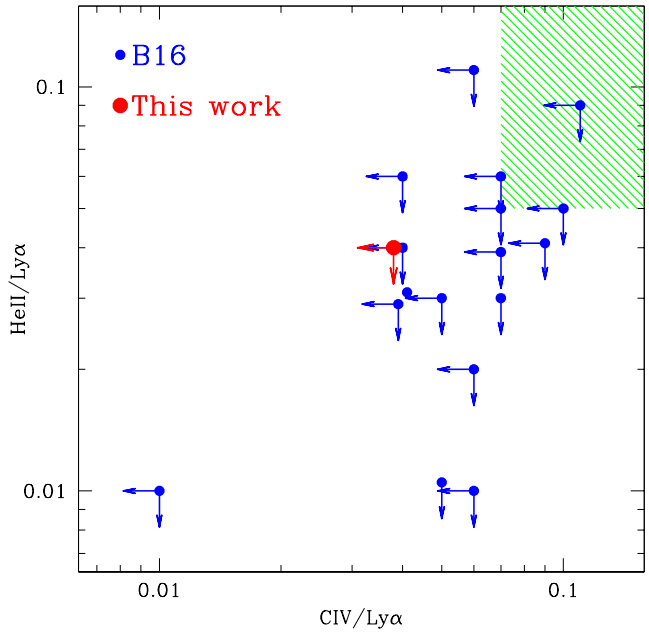

Fig. 13. Ratios of high-ionization line fluxes for our object (red) and for those of B16 (Table 2) surrounding radio-quiet QSOs (blue). The He II line is detected in only one object of the latter sample, while the C IV line is detected in three objects. The green hatched area represents the range of line ratios compatible with photoionization models (Arrigoni Battaia et al. 2015).

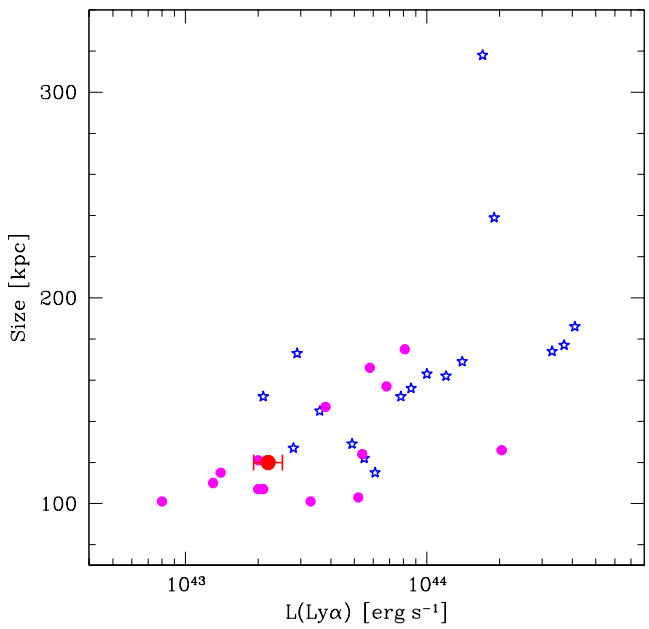

Fig. 14. Relation size–luminosity for our object (red) and for those of B16 that are radio quiet (blue). The magenta full dots represent the 14 giant LABs discovered by Matsuda et al. (2011).

of some Lyα emitters (LAEs). LAE 221745.3+002006, for instance, shows a very similar profile (Yamada et al. 2012, Fig. 2). The latter authors concluded from their observation of 91 LAEs that more than 40% of them show a double peak, and that in most cases the red component is stronger than the blue one, which is naturally explained by transfer effects in expanding media, even inhomogeneous ones (Verhamme et al. 2006, 2008, 2012; Gronke et al. 2016, 2017).

Its total Lyα flux is

$$F_{\mathrm{Ly}\alpha} = (7.6 \pm 0.4) \times 10^{-17}\ \mathrm{erg\ s^{-1}\ cm^{-2}}$$

and the positions and widths of the two peaks are summarized in Table 3. The emission wavelength of the red peak coincides closely (i.e., within 0.6 Å or 36 km s^{-1}) with the first moment of the emission line of the LAB surrounding the QSO. Thus, assuming that the double-peak appearance is due to transfer in an expanding medium, the unabsorbed line would be centered at about −230 km s^{-1} with respect to the LAB emission. Such a small velocity difference suggests that this LAE is indeed close to the QSO+LAB system.

At this point, the question arises whether LAE1 might owe at least part of its luminosity to photoionization by the QSO (fluorescence scenario). Even in the most extreme case of a purely external photoionizing source, a double peak similar to the observed peak would be produced (Cantalupo et al. 2005), but some continuum is detected, so it is difficult to conclude.

Yamada et al. (2012) observed 91 LAEs with a spectral resolution $R \simeq 1700$, very similar to that of MUSE. They show in their Fig. 5 the empirical relation between the velocity separation between the red and blue peaks and the FWHM of the stronger peak. Our LAE1 object has a rather small velocity separation (392 ± 36 km s^{-1}) for the width of the stronger (red) peak, sending its representative point onto the lower envelope defined by the objects of Yamada et al. (2012). It is also reminiscent of the Lyman continuum emitters (LCEs) examined by Verhamme et al. (2017).

Using Eq. (11) and the luminosity distance corresponding to the average redshift $z = 3.0855$, we obtain the luminosity

$$L_{\mathrm{Ly}\alpha} = (6.5 \pm 0.3) \times 10^{42}\ \mathrm{erg\ s^{-1}}.$$

We do not show any velocity or FWHM map for this emitter because of its small spatial extension.

In a white-light image (obtained by integrating the datacube over all wavelengths), we see a very faint object at the position of the Lyα emission, which confirms that we are not in the extreme case of the "dark galaxies" seen by Cantalupo et al. (2012). The rest-frame equivalent width (EW_0) obtained using the same five-pixels radius aperture for both the Lyα line and the continuum (broad band – 2000 Å – image reconstructed from the MUSE datacube and assuming a β slope of −2) is $EW_0 < 130$ Å, while a dark galaxy is defined by $EW_0 > 240$ Å. Therefore, LAE1 must be powered from inside, for instance, by some stellar formation, although we cannot exclude some contribution of fluorescence due to the QSO, as mentioned above.

The second object, LAE2, appears very similar to LAE1 although it is much fainter and less extended (Fig. 16, left panel). The blue component of the emission line seems brighter compared to the red component than it is in LAE1 (see Fig. 16, right panel), although it is also more affected by the noise[5]. LAE2 lies 26.5″ away from the QSO, representing a projected distance of 207 pkpc and also shares the same redshift as the LAB one. Its coordinates and characteristics are given in Table 3.

Its total Lyα flux within a 1.0″ radius is

$$F_{\mathrm{Ly}\alpha} = (12.0 \pm 1.2) \times 10^{-18}\ \mathrm{erg\ s^{-1}\ cm^{-2}}.$$

For the luminosity distance corresponding to the average redshift $z = 3.0869$, we obtain the luminosity

$$L_{\mathrm{Ly}\alpha} = (1.0 \pm 0.1) \times 10^{42}\ \mathrm{erg\ s^{-1}}.$$

[5] The spectrum is drawn here from a datacube from which continuum sources were subtracted, thereby avoiding contamination by galaxies close to the line of sight.

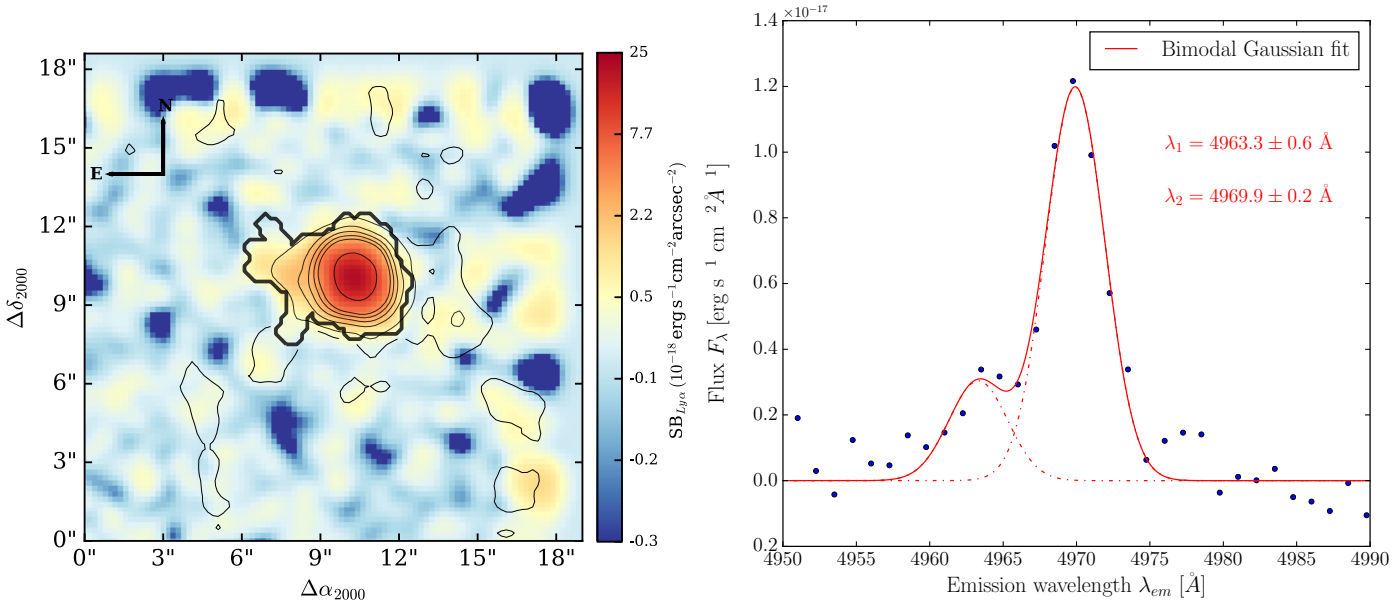

Fig. 15. *Left*: CubEx optimally extracted map of the probable Lyα emitter LAE1 located 34″ away from the QSO. The key to the curves is the same as for Fig. 10. *Right*: spectrum of the LAE1 object, summed on a disk with 2.0″ radius. The broad continuous curve shows a fit performed with a bimodal Gaussian functions. The continuum has been subtracted and the wavelengths are corrected to vacuum.

Table 3. Equatorial coordinates of the two LAEs detected at same redshift as the LAB.

Object	α (J2000) [h:m:s]	δ [°:′:″]	Peak	λ [Å]	z	*FWHM* [km s^{-1}]	*FWHM* [Å]	Δv [km s^{-1}]
LAE1	21:02:42.711	−35:52:42.7	blue	4963.3 ± 0.6	3.0828 ± 0.0005	284 ± 90	4.7 ± 1.5	−434 ± 36
			red	4969.9 ± 0.2	3.0882 ± 0.0001	287 ± 23	4.8 ± 0.4	−36 ± 12
LAE2	21:02:43.896	−35:52:42.6	blue	4963.4 ± 0.8	3.0828 ± 0.0006	284 ± 112	4.7 ± 1.9	−429 ± 48
			red	4972.9 ± 0.3	3.0906 ± 0.0002	348 ± 44	5.8 ± 0.7	145 ± 18

Notes. The central positions λ (corrected to vacuum) and FWHM of the two Gaussian fits to each LAE Lyα emission line are given as well. The Δv quantity is the velocity difference between the peak position and the first moment of the average Lyα profile of the LAB surrounding the QSO.

The rest-frame equivalent width of LAE2 has been estimated in a $r = 6$ pixels aperture at $EW_0 \simeq 17 \pm 4$ Å.

The blue peaks of LAE1 and LAE2 occur at exactly the same redshift, but this should be considered a mere coincidence, especially because for LAE1, the fit of the blue peak is very sensitive to noise because the two peaks are not clearly separated. The presence of these two LAEs in the field probably reflects the overdensity that is generally related with a QSO.

5.4. Starburst galaxy near the line of sight of the QSO

An emission line galaxy is detected about 5.5″ to the NW of the QSO. The H_α, H_β, [O II]λ3727, [O III]λ4959, 5007 lines are clearly identified, while the [N II]λ6584 line marginally so. The five stronger lines allow us to determine the redshift of this galaxy at $z = 0.33005 \pm 0.00009$.

We searched the QSO spectrum for a possible sodium absorption linked to this galaxy in the strong Na I D lines at 5889 Å and 5895 Å (rest frame). As one arcsecond corresponds to 4.8 pkpc at $z = 0.33$, the impact parameter is about 26 pkpc, and one may expect a non-negligible absorption if the galaxy is not too compact. We found a faint (2% depth) unresolved line at 7841.8 Å that might correspond to Na I λ5889 (which has the larger oscillator strength), but it is offset by a velocity $\Delta v = 280$ km s^{-1} with respect to the expected redshifted line. If this feature really were the Na I λ5889 line, then it would correspond to a Na I column density on the order of 10^{11} cm^{-2}. If all Na were neutral and none of it were locked in dust, this would correspond to an H column density of about 10^{17} cm^{-2} for solar metallicity. These numbers appear reasonable in view of the Na column densities (6×10^{11} cm^{-2} to 5×10^{13} cm^{-2}) found by Schwartz & Martin (2004) for local dwarf starburst galaxies; however, the non-detection of the Na Iλ5895 line makes the above estimates a speculation.

We now focus on other properties of this galaxy. The Balmer decrement can be estimated through the ratio $H_\alpha/H_\beta \simeq 2.71$: it is slightly lower than the usually adopted value of 2.86, suggesting no significant dust reddening. The [N II]λ6584/H_α and [O III]λ5007/H_β ratios point to a rather typical star-forming galaxy (see e.g. Lamareille et al. 2004, Fig. 1). It has a relatively high excitation: with a ratio [O III]λ5007/[O II]λ3727 = 3.46, it resembles the galaxies of the DR7 sample of Stasińska et al. (2015), although the [O III]λ4363 line is not clearly detected. The [O III]/[O II] ratio, although rather high, is lower than that of the LCEs of Verhamme et al. (2017). Its properties are listed in Table 4 and its spectrum is shown in Fig. 17.

The oxygen abundance can be estimated from the line strengths given in Table 4 and from the O3N2 $\equiv \log\left(\frac{[\mathrm{O\,III}]\lambda5007/\mathrm{H}_\beta}{[\mathrm{N\,II}]\lambda6584/\mathrm{H}_\alpha}\right)$ and N2 $\equiv \log([\mathrm{N\,II}]\lambda6584/\mathrm{H}_\alpha)$ criteria (Marino et al. 2013, Eqs. (2) and (4), respectively). The main

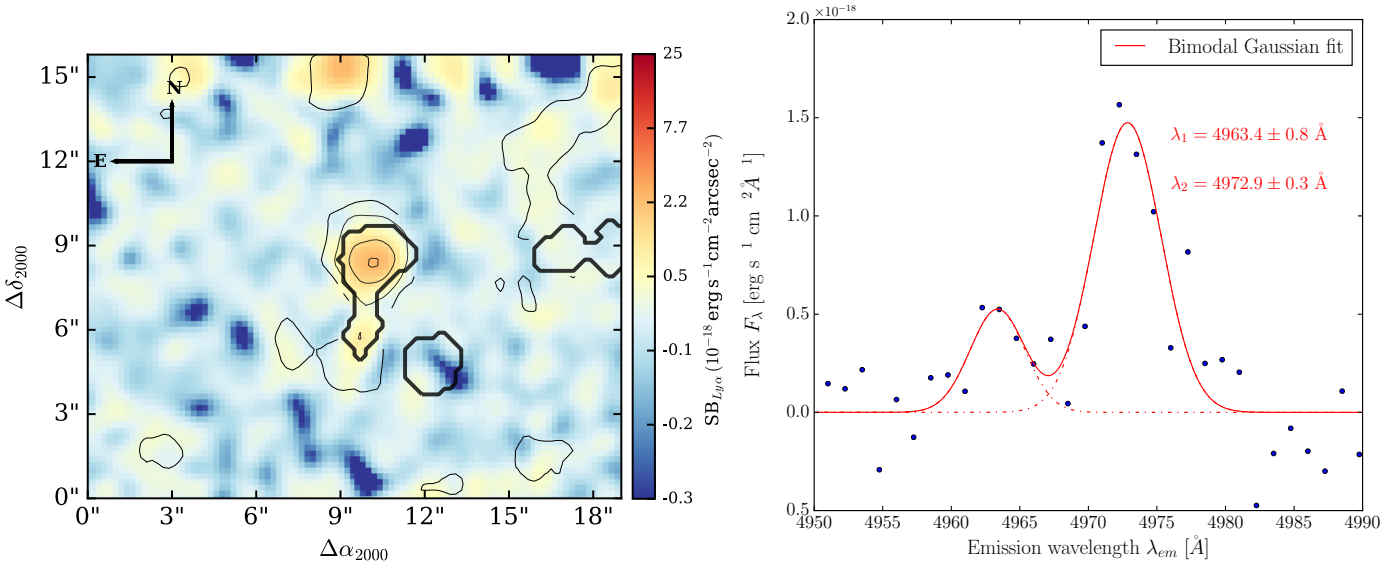

Fig. 16. *Left*: same as Fig. 15, but for LAE2. *Right*: same as Fig. 15, but for LAE2. The spectrum is summed over a disk with 1.0″ radius.

Table 4. Equatorial coordinates and line intensities of the starburst galaxy at $z = 0.33$.

α_{J2000} [h:mn:s]	δ_{J2000} [°:′:″]
21:02:44.316	−35:53:02.55
Line	Observed flux [10^{-18} erg s^{-1} cm^{-2}]
[O II]3727	18.1
H_β	14.9
[O III]4959	20.1
[O III]5007	62.6
H_α	40.3
[N II]6584	~2.3

uncertainty, about a factor of two, lies in the [N II]λ6584 line intensity. We obtain

$$12 + \log(\mathrm{O/H}) = 8.13 \pm 0.07 \quad (\mathrm{O3N2}) \tag{15}$$

$$= 8.17 \pm 0.14 \quad (\mathrm{N2}), \tag{16}$$

assuming a ±0.3 dex error on both criteria. This corresponds to [O/H] ∼ −0.6 assuming a solar oxygen abundance of 8.69 (Allende Prieto et al. 2001), and agrees well with local starburst galaxies (Lee & Skillman 2004; Fensch et al. 2016; Hirschauer et al. 2015; Izotov et al. 2014).

6. To which object does the LAB belong?

Interestingly, the overall spectral shape of the central part of the LAB displayed in Fig. 6 is asymmetric, with a steep blue side and a less abrupt red side. This typically results from radiative transfer in the interstellar matter (ISM) of LAE galaxies (see, e.g., Fig. 13 of Kashikawa et al. 2011 and Fig. 5 of Hu et al. 2010). This shape is generally interpreted as the result of radiative transfer in an expanding medium (Verhamme et al. 2008; Hashimoto et al. 2015; Karman et al. 2017; Yang et al. 2017a).

The crucial point here is that in case of transfer in an expanding medium, the peak of the Lyα emission is shifted to the red with respect to the systemic velocity of the emitting galaxy (Yang et al. 2017b; Erb et al. 2014). Furthermore, the shift is roughly proportional to the H I column density (Hashimoto et al. 2015, Fig. 11). Now, when we consider the relative velocities of

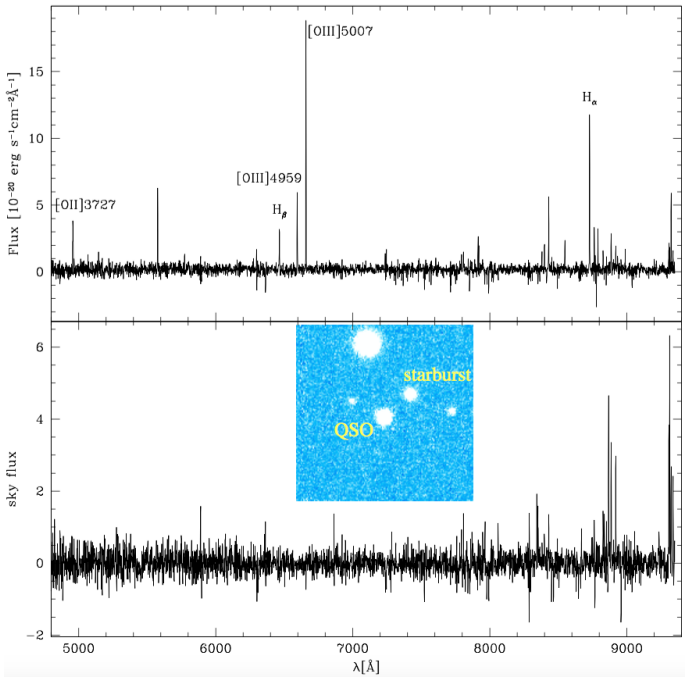

Fig. 17. MUSE spectrum of the starburst galaxy (*top*) and spectrum of a nearby sky background (*bottom*). The brightest lines are identified. The very bright [O I] λ5577.34 telluric line appears, by chance, in the galaxy spectrum but not in the sky spectrum, because it is not subtracted correctly in most parts of the datacube. The *inset* is the monochromatic MUSE image at 6658.75 Å (redshifted [O III] λ5007) centered on the QSO, showing the position of the emission line galaxy; the image is 30″ across; the bright object near the top is a Galactic red giant star.

the PDLA, LAB, and QSO as summarized in Fig. 18, we see that the average LAB emission line lies redward of the PDLA, but blueward of the QSO[6] (even when we admit $z_{\mathrm{QSO}} = 3.092$, which would place it at $v = 714\,\mathrm{km\,s^{-1}}$). However, in the case of an expanding medium centered on the QSO, one would expect the reverse, namely the QSO to lie *blueward* of the LAB emission line. The respective positions of the PDLA and the

[6] An earlier version of this figure has been published by Leibundgut & Robertson (1999, Fig. 6).

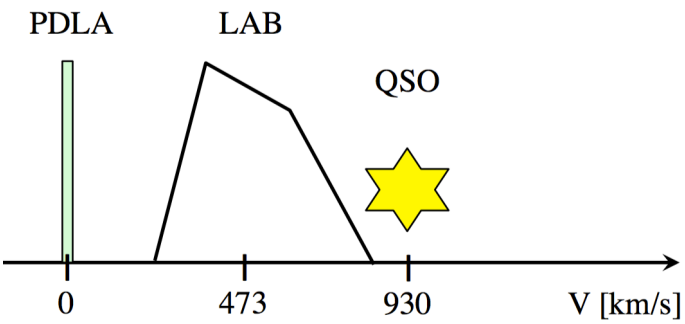

Fig. 18. Schematic view of the positions of the PDLA, LAB, and QSO along the velocity axis. The PDLA redshift (determined with metallic lines) was adopted as the origin because of its excellent precision. The QSO lies beyond the LAB, while the asymmetry of the LAB emission line would suggest the reverse when we assume the model of a QSO that is surrounded by an expanding medium.

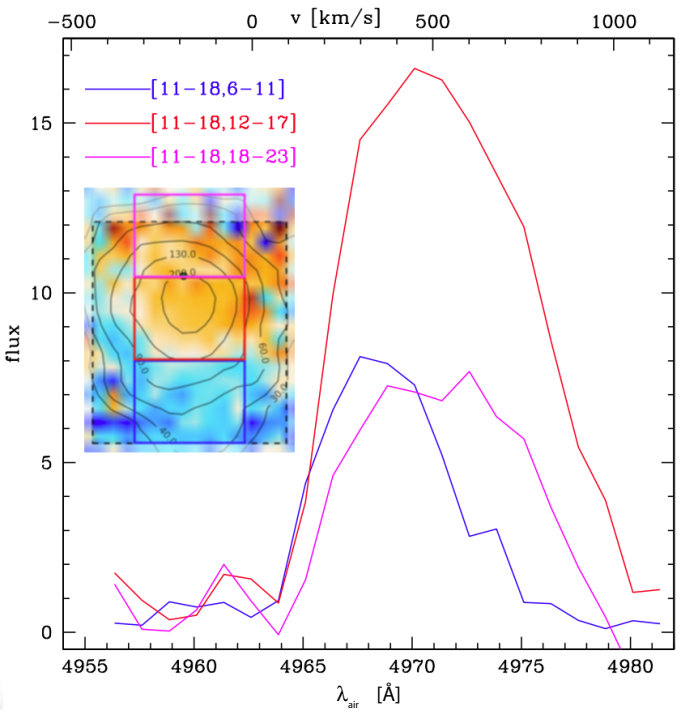

Fig. 19. Lyα line profiles spatially integrated on rectangles covering 8×6 spaxels. The coordinates of the lower left and upper right corners of the rectangles are given, the [1, 1] spaxel being the lower left one in each panel of Fig. 8; the positions of the rectangles are also shown in the inset. The blue, red, and magenta curves refer to the southern, middle, and northern rectangle, respectively.

LAB are quite consistent with an expanding medium centered on the PDLA rather than on the QSO. This is true even quantitatively, since according to the hydrogen column density versus Lyα line redshift relation mentioned above, we have $\Delta v \sim 400-500\,\mathrm{km\,s^{-1}}$ for the PDLA column density $\log N(\mathrm{H\,I}) = 20.9$ found in Eq. (8); this is fully consistent with the $\sim$470 km s^{-1} shift we see in Fig. 18.

Thus far, we have neglected the details of the "velocity" field displayed in Fig. 8 and assumed that the bright central part of the LAB can be interpreted as an unresolved expanding medium. To explore how far the Lyα line asymmetry depends on position within the LAB, we show in Fig. 19 the line spatially integrated on three 8×6 spaxel rectangles that are arranged contiguously from south to north; the first rectangle covers negative velocities (see Fig. 8), while the other two, lying just to the south and to the north of the QSO, cover positive velocities. In spite of the overall velocity difference, each Lyα profile displays a similar asymmetry, with a steep blue side and a more gradual red side. Thus, the skewness of the average line (integrated on the whole LAB) cannot be explained by the addition of symmetric lines shifted according to the velocity field, and the expanding medium picture remains essentially valid.

Another completely independent argument in favor of a PDLA-centered LAB stems from a remark by Hennawi et al. (2009) about a similar object, J1240+1455: under the assumption of an LAB centered on the QSO and lying, therefore, *behind* the galaxy acting as the PDLA, one would expect to see the PDLA galaxy *in silhouette* against the bright nebular background. In other words, the PDLA galaxy would extinct not only the QSO point source, but also part of the LAB, unless it is so compact as to subtend only a small fraction of an arcsecond, that is, much less than the seeing disk. Our observations provide no sign of any extended dark region in the very center of the LAB that would betray the presence of a large, that is, $\sim$10 kpc scale, absorbing galaxy. Although the average size of late-type galaxies at $z = 3$ is in the range $0.15''-0.5''$ (Ferguson et al. 2004; van der Wel et al. 2014), it is based on the UV continuum; one can expect that the H I size is larger, maybe on the order of the seeing, so that such a galaxy would leave an observable footprint.

Therefore, assuming that the H I and metal line absorptions do correspond to the systemic velocity of the PDLA galaxy, there are strong indications that the LAB surrounds the latter rather than the QSO. This would correspond to the model (i) envisaged by Leibundgut & Robertson (1999, Sect. 4.5). This conclusion is all the more unexpected, because each of the 17 radio-quiet quasars observed by B16 is surrounded by an LAB. Why our object should prove an exception remains an open question, although the presence of the PDLA may betray past interactions that resulted in a "naked" QSO like HE0450-2958 (Magain et al. 2005; Elbaz et al. 2009).

7. Conclusion

We have performed an integral-field spectroscopic study of the neighborhood of a radio-quiet QSO at redshift $z = 3.095$. An emission feature at $z = 3.0887$ is present within the damped Lyman absorption trough of the QSO spectrum and is spatially located along its line of sight. According to a previous study (Leibundgut & Robertson 1999), this emission feature is probably a Lyman α blob, although it was not clear to the authors whether it is powered by the QSO or by the PDLA. We adapted the method of spectral subtraction of the QSO component, first proposed by Leibundgut & Robertson (1999), to the MUSE datacube in order to isolate the LAB contribution down to the position of the QSO itself. We confirm that the blob presents a sharp velocity gradient with a contrast of $\sim$200 km s^{-1} close to the line of sight to the QSO (Figs. 8 and 11).

Moreover, we found that the LAB is much more extended than thought so far, with a filament protruding to the south, so that its total extent reaches $\sim$120 kpc. The latter result at first sight confirms the finding of B16 that all radio quiet QSOs at $3 < z < 4$ are surrounded by an LAB, the total extension of which reaches 100 kpc or more. The luminosity of our LAB is also quite typical, even though it lies near the faint end. Furthermore, like B16, we found no sign of violent kinematics: the FWHM of the Lyα line is always well below 1000 km s^{-1}, unlike the LABs surrounding high-z radio galaxies. The upper limits we found on the intensity of high-ionization lines also compare well

with B16. The surface brightness profile is compatible with a power-law profile, with a slope similar to (but slightly shallower than) the typical slope found by B16. However, the asymmetry of the average LAB emission line suggests that the emitting nebula is centered on the PDLA galaxy rather than on the QSO because the QSO spectrum lies redward, not blueward of the LAB emission. Furthermore, we found no sign of any significantly extended dark region in the very center of the LAB that would betray the presence of the PDLA galaxy in the foreground, in front of a QSO-centered LAB that would lie in the background. This makes the comparison with the B16 objects less straightforward and suggests that our object may be rather uncommon.

Two other LAEs were found close to the NW corner of the MUSE field of view, at projected distances of 34″ (265 kpc) and 26.5″ (207 kpc) from the QSO. Although the lack of other emission lines in the MUSE spectral range leaves some ambiguity, the typical double profile of the single line, together with a redshift coinciding perfectly with that of the central LAB, make their Lyα identification most probable. These other emitters do not seem to be just other Lyα blobs that would be powered by the QSO only because the equivalent width of their emission line does not exceed the rest-frame equivalent width limit ($EW_0 > 240$ Å) required to classify them as protogalactic clouds or dark galaxies (Cantalupo et al. 2012).

We provided the properties of the PDLA, confirming the H I column density found previously by Leibundgut & Robertson (1999) with a completely different instrumental setup.

Acknowledgements. We thank the ESO staff for having made this observation possible. This research has made use of the SIMBAD database operated at CDS, Strasbourg, France. R.A.M. acknowledges support by the Swiss National Science Foundation. M.H. acknowledges the support of the Swedish Research Council (Vetenskapsrådet) and the Swedish National Space Board (SNSB), and is a Fellow of the Knut and Alice Wallenberg Foundation. S.C. gratefully acknowledges support from Swiss National Science Foundation grant PP00P2_163824. A.V. is supported by a Marie Heim Vögtlin fellowship of the Swiss National Science Foundation.

References

Allende Prieto, C., Lambert, D. L., & Asplund, M. 2001, ApJ, 556, L63
Arrigoni Battaia, F., Yang, Y., Hennawi, J. F., et al. 2015, ApJ, 804, 26
Bennett, C. L., Larson, D., Weiland, J. L., & Hinshaw, G. 2014, ApJ, 794, 135
Borisova, E., Cantalupo, S., Lilly, S. J., et al. 2016, ApJ, 831, 39
Bunker, A., Smith, J., Spinrad, H., Stern, D., & Warren, S. 2003, Ap&SS, 284, 357
Cantalupo, S., Porciani, C., Lilly, S. J., & Miniati, F. 2005, ApJ, 628, 61
Cantalupo, S., Lilly, S. J., & Porciani, C. 2007, ApJ, 657, 135
Cantalupo, S., Lilly, S. J., & Haehnelt, M. G. 2012, MNRAS, 425, 1992
Cantalupo, S., Arrigoni-Battaia, F., Prochaska, J. X., Hennawi, J. F., & Madau, P. 2014, Nature, 506, 63
Carswell, R. F., & Webb, J. K. 2014, Astrophysics Source Code Library [record ascl: 1408.015]
Christensen, L., Jahnke, K., Wisotzki, L., & Sánchez, S. F. 2006, A&A, 459, 717
Ciddor, P. E. 1996, Appl. Opt., 35, 1566
Davis, T. M., & Scrimgeour, M. I. 2014, MNRAS, 442, 1117
Dijkstra, M., & Kramer, R. 2012, MNRAS, 424, 1672
Dijkstra, M., & Loeb, A. 2008, MNRAS, 386, 492
Dijkstra, M., & Loeb, A. 2009, MNRAS, 400, 1109
Elbaz, D., Jahnke, K., Pantin, E., Le Borgne, D., & Letawe, G. 2009, A&A, 507, 1359
Ellison, S. L., Yan, L., Hook, I. M., et al. 2002, A&A, 383, 91
Ellison, S. L., Prochaska, J. X., Hennawi, J., et al. 2010, MNRAS, 406, 1435
Erb, D. K., Bogosavljević, M., & Steidel, C. C. 2011, ApJ, 740, L31
Erb, D. K., Steidel, C. C., Trainor, R. F., et al. 2014, ApJ, 795, 33
Fardal, M. A., Katz, N., Gardner, J. P., et al. 2001, ApJ, 562, 605
Fensch, J., Duc, P.-A., Weilbacher, P. M., Boquien, M., & Zackrisson, E. 2016, A&A, 585, A79
Ferguson, H. C., Dickinson, M., Giavalisco, M., et al. 2004, ApJ, 600, L107
Francis, P. J., & McDonnell, S. 2006, MNRAS, 370, 1372
Geach, J. E., Alexander, D. M., Lehmer, B. D., et al. 2009, ApJ, 700, 1
Gronke, M., Dijkstra, M., McCourt, M., & Oh, S. P. 2016, ApJ, 833, L26
Gronke, M., Dijkstra, M., McCourt, M., & Oh, S. P. 2017, A&A, submitted [arXiv:1704.06278]
Haiman, Z., & Rees, M. J. 2001, ApJ, 556, 87
Haiman, Z., Spaans, M., & Quataert, E. 2000, ApJ, 537, L5
Hashimoto, T., Verhamme, A., Ouchi, M., et al. 2015, ApJ, 812, 157
Hayes, M., Scarlata, C., & Siana, B. 2011, Nature, 476, 304
Heckman, T. M., Lehnert, M. D., Miley, G. K., & van Breugel, W. 1991, ApJ, 381, 373
Hennawi, J. F., Prochaska, J. X., Kollmeier, J., & Zheng, Z. 2009, ApJ, 693, L49
Hennawi, J. F., Prochaska, J. X., Cantalupo, S., & Arrigoni-Battaia, F. 2015, Science, 348, 779
Herenz, E. C., Wisotzki, L., Roth, M., & Anders, F. 2015, A&A, 576, A115
Hirschauer, A. S., Salzer, J. J., Bresolin, F., Saviane, I., & Yegorova, I. 2015, AJ, 150, 71
Hu, E. M., & Cowie, L. L. 1987, ApJ, 317, L7
Hu, E. M., Cowie, L. L., Barger, A. J., et al. 2010, ApJ, 725, 394
Husemann, B., Wisotzki, L., Sánchez, S. F., & Jahnke, K. 2013, A&A, 549, A43
Izotov, Y. I., Guseva, N. G., Fricke, K. J., & Henkel, C. 2014, A&A, 561, A33
Karman, W., Caputi, K. I., Caminha, G. B., et al. 2017, A&A, 599, A28
Kashikawa, N., Shimasaku, K., Matsuda, Y., et al. 2011, ApJ, 734, 119
Lamareille, F., Mouhcine, M., Contini, T., Lewis, I., & Maddox, S. 2004, MNRAS, 350, 396
Lee, H.-W., & Ahn, S.-H. 1998, ApJ, 504, L61
Lee, H., & Skillman, E. D. 2004, ApJ, 614, 698
Lehnert, M. D., & Becker, R. H. 1998, A&A, 332, 514
Leibundgut, B., & Robertson, J. G. 1999, MNRAS, 303, 711
Magain, P., Letawe, G., Courbin, F., et al. 2005, Nature, 437, 381
Marino, R. A., Rosales-Ortega, F. F., Sánchez, S. F., et al. 2013, A&A, 559, A114
Martin, D. C., Chang, D., Matuszewski, M., et al. 2014a, ApJ, 786, 106
Martin, D. C., Chang, D., Matuszewski, M., et al. 2014b, ApJ, 786, 107
Martin, D. C., Matuszewski, M., Morrissey, P., et al. 2015, Nature, 524, 192
Matsuda, Y., Yamada, T., Hayashino, T., et al. 2004, AJ, 128, 569
Matsuda, Y., Nakamura, Y., Morimoto, N., et al. 2009, MNRAS, 400, L66
Matsuda, Y., Yamada, T., Hayashino, T., et al. 2011, MNRAS, 410, L13
Mori, M., Umemura, M., & Ferrara, A. 2004, ApJ, 613, L97
North, P. L., Courbin, F., Eigenbrod, A., & Chelouche, D. 2012, A&A, 542, A91
Prescott, M. K. M., Kashikawa, N., Dey, A., & Matsuda, Y. 2008, ApJ, 678, L77
Prochaska, J. X., Hennawi, J. F., & Herbert-Fort, S. 2008, ApJ, 675, 1002
Richard, J., & Bacon, R. 2014, MUSE User manual, VLT-MAN-MUS-14670-1477, ESO
Richards, G. T. 2001, ApJS, 133, 53
Richards, G. T., Kruczek, N. E., Gallagher, S. C., et al. 2011, AJ, 141, 167
Rosdahl, J., & Blaizot, J. 2012, MNRAS, 423, 344
Rybicki, G. B., & Loeb, A. 1999, ApJ, 520, L79
Schwartz, C. M., & Martin, C. L. 2004, ApJ, 610, 201
Smith, D. J. B., & Jarvis, M. J. 2007, MNRAS, 378, L49
Stasińska, G., Izotov, Y., Morisset, C., & Guseva, N. 2015, A&A, 576, A83
Steidel, C. C., Adelberger, K. L., Shapley, A. E., et al. 2000, ApJ, 532, 170
Taniguchi, Y., & Shioya, Y. 2000, ApJ, 532, L13
Trebitsch, M., Verhamme, A., Blaizot, J., & Rosdahl, J. 2016, A&A, 593, A122
van Breugel, W., de Vries, W., Croft, S., et al. 2006, Astron. Nachr., 327, 175
Vanden Berk, D. E., Richards, G. T., Bauer, A., et al. 2001, AJ, 122, 549
van der Wel, A., Franx, M., van Dokkum, P. G., et al. 2014, ApJ, 788, 28
Verhamme, A., Schaerer, D., & Maselli, A. 2006, A&A, 460, 397
Verhamme, A., Schaerer, D., Atek, H., & Tapken, C. 2008, A&A, 491, 89
Verhamme, A., Dubois, Y., Blaizot, J., et al. 2012, A&A, 546, A111
Verhamme, A., Orlitová, I., Schaerer, D., & Hayes, M. 2015, A&A, 578, A7
Verhamme, A., Orlitová, I., Schaerer, D., et al. 2017, A&A, 597, A13
Villar-Martín, M., Vernet, J., di Serego Alighieri, S., et al. 2003, MNRAS, 346, 273
Warren, S. J., Hewett, P. C., & Osmer, P. S. 1991, ApJS, 76, 23
Weidiger, M., Moller, P., Fynbo, J. P. U., & Thomsen, B. 2005, A&A, 436, 825
Willott, C. J., Chet, S., Bergeron, J., & Hutchings, J. B. 2011, AJ, 142, 186
Wisotzki, L., Bacon, R., Blaizot, J., et al. 2016, A&A, 587, A98
Wright, E. L. 2006, PASP, 118, 1711
Yamada, T., Matsuda, Y., Kousai, K., et al. 2012, ApJ, 751, 29
Yang, Y., Zabludoff, A., Tremonti, C., Eisenstein, D., & Davé, R. 2009, ApJ, 693, 1579
Yang, Y., Zabludoff, A., Jahnke, K., & Davé, R. 2014, ApJ, 793, 114
Yang, H., Malhotra, S., Gronke, M., et al. 2017a, ApJ, submitted [arXiv:1701.01857]
Yang, H., Malhotra, S., Rhoads, J. E., et al. 2017b, ApJ, 838, 4